REGULATION OF ACTOMYOSIN ATPASE

by

Jinghua Ge

A dissertation submitted to the faculty of
The University of North Carolina at Charlotte
in partial fulfillment of the requirements
for the degree of Doctor of Philosophy in
Optical Science and Engineering

Charlotte

2016

Approved by:

_____
Dr. Yuri Nesmelov

_____
Dr. Faramarz Farahi

_____
Dr. Donald Jacobs

_____
Dr. Tsing-Hua Her

_____
Dr. Jerry Troutman

ABSTRACT

JINGHUA GE. Regulation of actomyosin ATPase
(Under the direction of DR. YURI NESMELOV)

Myosin is a molecular motor that converts chemical energy to mechanical energy, thus generating force and movement in muscles and cells. Myosin interacts with two ligands, ATP (fuel) and actin filaments (motor's tracks). Actomyosin interaction is regulated by the availability of ATP and by the proteins specifically binding actin or myosin. We would like to know how else myosin can be regulated. In this dissertation, we have examined actomyosin regulation by (a) metal ions, complexed with ATP, (b) crowding of actomyosin environment, and (c) ionic strength of actomyosin solution. We have used steady state myosin ATPase activity measurements, myosin intrinsic fluorescence, fluorescence of pyrene labeled actin and home-built transient time-resolved Förster resonance energy transfer to monitor myosin and actomyosin kinetics.

We have perturbed myosin nucleotide binding site with magnesium-, manganese-, or calcium-nucleotide complexes, using metal cation as a probe to examine the pathways of myosin ATPase in the presence of actin. We found that actin activation of myosin ATPase does not depend on metal cation, regardless of the cation-specific kinetics of nucleotide binding and dissociation. The rate limiting step of myosin ATPase depends on the metal cation. The rate of the recovery stroke and the reverse recovery stroke is directly proportional to the ionic radius of the cation. The rate of nucleotide release from myosin and actomyosin, and ATP binding to actomyosin depends on the cation coordination number.

To emulate the effect of crowding in cells, we studied actomyosin cycle reactions in the presence of a high-molecular-weight polymer, Ficoll70. We observed an increase in the maximum velocity of the actomyosin ATPase cycle, and our transient-kinetics

experiments showed that virtually all individual steps of the actomyosin cycle were affected by the addition of Ficoll70. The observed effects of macromolecular crowding on the myosin-ligand interaction cannot be explained by the increase of a solute's chemical potential. A time-resolved Förster resonance energy transfer experiment confirmed that the myosin head assumes a more compact conformation in the presence of Ficoll70 than in a dilute solution. We conclude that the crowding-induced myosin conformational change plays a major role in the changed kinetics of actomyosin ATPase.

The rate of actin and myosin rigor binding depends on the ionic strength of the solution, confirming that actomyosin interaction is electrostatically driven. The dependence of the rate of actin and myosin interaction on the ionic strength of the solution reflects the charge of the interface of the interacting molecules. We used recent data on the structure of actomyosin complex to determine the charge and charge distribution of the actin binding interface of myosin head. The experimental transient kinetics data and the computational analysis were used to compare cellular and muscle myosin in terms of similarities and differences of their actin binding interface.

In summary, the results of this study suggest that cross-bridge kinetics, and therefore muscle performance, significantly depends on intracellular environments. What we have learned in this study is essential not only for revealing movement at the cellular and molecular levels but also for enhancing muscle power output from environments.

ACKNOWLEDGEMENTS

I am very grateful to my advisor Prof. Yuri Nesmelov for his academic supervision through all my PhD study. During these years of study, I am always inspired by his rigorous thinking, as well as the great enthusiasm in research. I appreciate very much the valuable suggestions and advices from my committee members, Prof. Faramarz Farahi, Prof. Donald Jacobs, Prof. Tsing-Hua Her, and Prof. Jerry Troutman. I would like to thank our collaborators, from University of Arizona (Prof. Andrei Astashkin) and Kazan State Power Engineering University (Prof. Tamara Serebrennikova), who have contributed analytic tools and designed research for this dissertation work. I would also like to thank all group members and/or research partners I have met in Charlotte: Prof. Irina Nesmelova, Dr. Yaroslav Tkachev, Dr. Furong Huang, Sherry Bouriyaphone, Bhavana Ambil and Marc Kankolongo Kabengele. I am thankful for the financial supports from National Institutes of Health Grants (AR059621, HL132315), as well as the GASP financial award offered by University of North Carolina at Charlotte. Without the kindly encouragement and support from my family, friends and fellow group members, this dissertation work would not have been possible.

TABLE OF CONTENTS

LIST OF FIGURES

LIST OF TABLES

CHAPTER 1: INTRODUCTION

1.1 Introduction of Molecular Motors

Molecular motors are enzymes with the ability of converting energy into motion or mechanical power (1). Molecular motors carry out various tasks such as muscle contraction, cell division, cell movement or sustain cell shape. These motors are ubiquitous to eukaryotic cells, and can be grouped into 35 classes based on sequence homology of their head domains as shown in Figure 1-1 (2). Types II are in the scope of the present thesis.

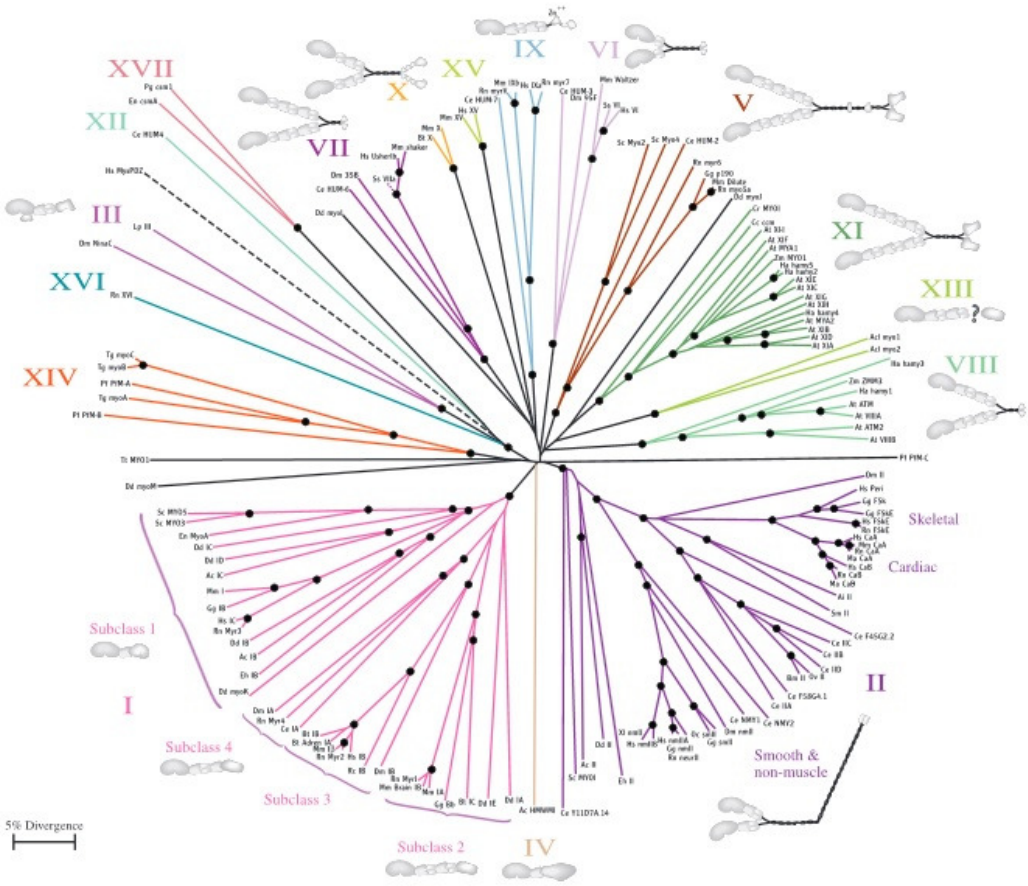

Figure 1-1: Myosin tree from Hodge and Cope(2)

Despite the large functional variety of myosins, they share a common mechanism. Here we used myosin II as an example to show the structure of myosin (Figure 1-2). Myosin II consists of two heavy chains (~220 kDa each) that dimerize at their tail region, and four light chains (two essential and two regulatory, ~20 kDa each). The N-terminal regions of the heavy chains create the catalytic motor domains, which is followed by a neck region. The neck is variable in length, and contains the binding sites of the light chains. The two α-helices of the heavy chains create a coiled-coil rod, the tail region.

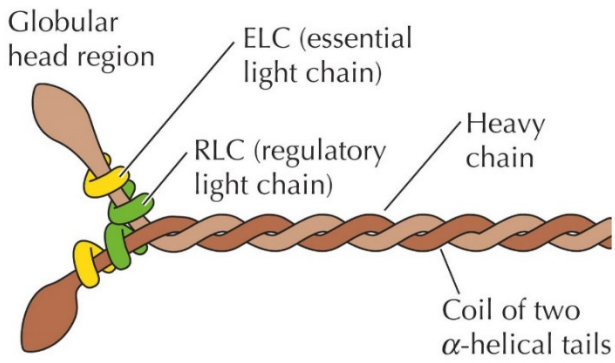

Figure 1-2: Myosin II- skeletal muscle dimer

1.2 Myosin ATPase Cycle

The mechanism of myosin ATPase could be represented with a simplified flowchart of the motor cycle(3) as shown in Figure 1-3. This model is an updated version of the chemomechanical model proposed by Lymn and Taylor (4).

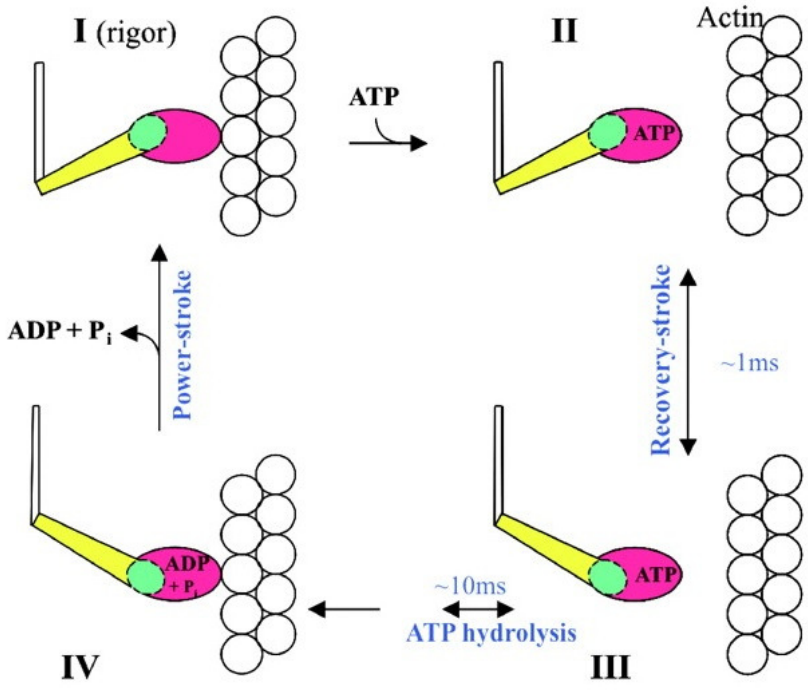

Figure 1-3: The actomyosin contraction cycle (3). The myosin head fragment is represented in colors. Red: motor domain, Green: hinge, Yellow: lever arm or neck.

The upper left corner of the figure shows a "rigor" (nucleotide-free) actomyosin interaction. Upon ATP binding the actin affinity of the myosin head decreases dramatically and the myosin rapidly releases actin (I-II). A reversible conformational transition follows (II-III). This is the "cocking" of the myosin. The resulting conformation (III) is competent for hydrolysis of the bound ATP. After hydrolysis, the residual myosin-products complex rebinds to actin (III-IV). Finally, the products (Pi and then ADP) sequentially dissociate from the nucleotide binding site. Product dissociation is linked to the so-called power-stroke, the directional pull on the actin filament.

Figure 1-4 shows a more detailed biochemical scheme of the myosin working cycle. The upper row of reactions represents the actin-bound states while the lower row shows the detached myosin. Every step is thermodynamically more or less reversible. However, ATP binding to the myosin head and Pi release after keep the cycle going into one direction. The main trajectory is highlighted in the box on Figure 1-4.

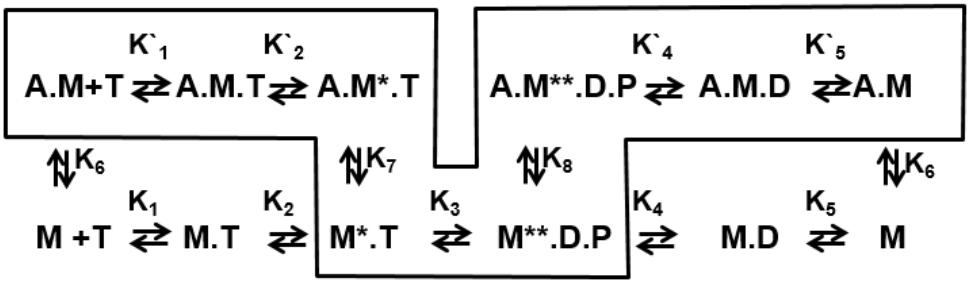

Figure 1-4: Kinetically resolved steps of the actomyosin ATPase cycle.
M - myosin; T - ATP; D - ADP; P - phosphate; M* - myosin in the pre-recovery stroke structural state; M** - myosin in the post-recovery stroke structural state.

1.3 Objectives

Myosin, usually in association with actin, is responsible for movements. Study the regulation of actin and myosin is essential not only for revealing movement at the cellular and molecular levels but also for directly increasing muscle power output in a diseased muscle. Actomyosin interaction is regulated by the availability of ATP and by the proteins specifically binding actin or myosin. In this dissertation, we were interested in how to regulate actomyosin performance, and examined these three different approaches (a) metal ions, complexed with ATP, (b) crowding of actomyosin environment, and (c) ionic strength of actomyosin solution. They would be discussed in Chapter IV, Chapter V and Chapter VI respectively. The results from this study suggest significant effects on cross-bridge kinetics by different intracellular environments, thus regulating muscle protein performance.

CHAPTER 2: MATERIAL AND METHODS

2.1 Protein Expression and Purification

In order to carry out a precise analysis of protein structure and function, it is necessary to isolate it from the cell and study it in purified form. In this chapter, purification of myosin and actin would be introduced. We worked with two types of myosin- skeletal and cellular. Myosin motor domain from *Dictyostelium discoideum* cell would be the source of cellular myosin. At the meantime, rabbit skeletal muscle from leg and back would be the source of skeletal muscle for skeletal myosin and actin prep.

Purification of any protein involves a series of steps designed to remove other proteins with physical properties differing from those of the protein of interest. In short words, purification of skeletal myosin and actin from rabbit muscle based on differential salt extraction. And purification of *D. discoideum* myosin employed Talon affinity resin followed by gradient elution.

2.2 Cellular Myosin Expression, Purification, and Labeling

2.2.1 *Dictyostelium Discoideum* Cells Culture

Dictyostelium discoideum is inexpensive and relatively easy to grow, it has been widely used to study a variety of fundamental biological processes(5). The cells can be grown in a standard microbiology incubator or on the laboratory bench provided that the room temperature is kept constant at approximately 22 °C.

Axenic culture employed HL5 medium(6): 10 g Dextrose (glucose), 5 g Yeast extract, 5 g Peptic peptone B, 5 g Proteose peptone, 0.66 g $Na_2HPO_4*7H_2O$, 1.2 g

KH_2PO_4 for each liter. Mix dextrose and DI water in a beaker until completely dissolving. Add peptones and yeast slowly to avoid dust cloud. Add potassium phosphate and sodium phosphate last. Bring to volume and adjust pH to 6.5. Autoclave for 30 minutes at 121°C to sterilize. Cool down to room temperature before adding 10 µg/ml G418 for selection.

A639C:K498C mutant of *D. discoideum* myosin motor domain was constructed and purified as described (7-9). Axenic growth for large-scale preparations, either stationary in plastic dishes or shaking in suspension, is the most common method to culture *D. discoideum*(5). It is important that they remain in an exponential growth phase (between 1×10^4 to 4×10^7 cells ml-1) rather than diluting to lower cell densities or allowing them to reach stationary phase. It is good practice to maintain a regular schedule for splitting the cultures to ensure a healthy cell population. Cell lines started from frozen stock. *D. discoideum* spores. Gently mix the cells with the medium to obtain an even distribution. We first start with a 100mm/10mL media dish, grow cell until confluent, then transfer to 150mm/20mL media dish, and grow until confluent, then transfer to a flask. Grow at room temperature. Cells will attach to the plastic surface and can be observed with a standard microscope, as shown in Figure 2-1.

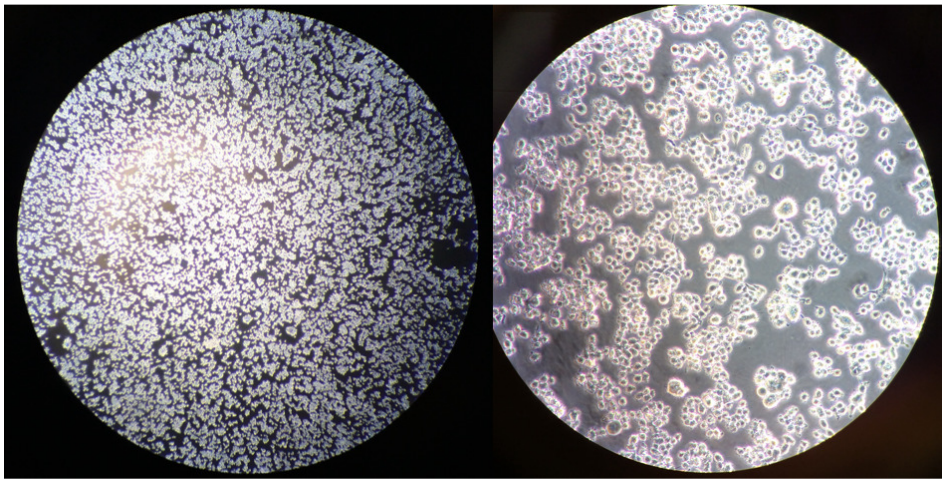

Figure 2-1: *D. discoideum* cells with microscope (Olympus CKX41) ×40 (Left) and ×200 (Right) magnification

Transfer cells to 500 ml flask with 100ml media in 3 days, then split into three 500 ml flasks with 100ml media in 3 days, continue with 2 liters flask with 500 ml media and 6 liters flask with 2 liters media transferring in each 3 days (Figure 2-2).

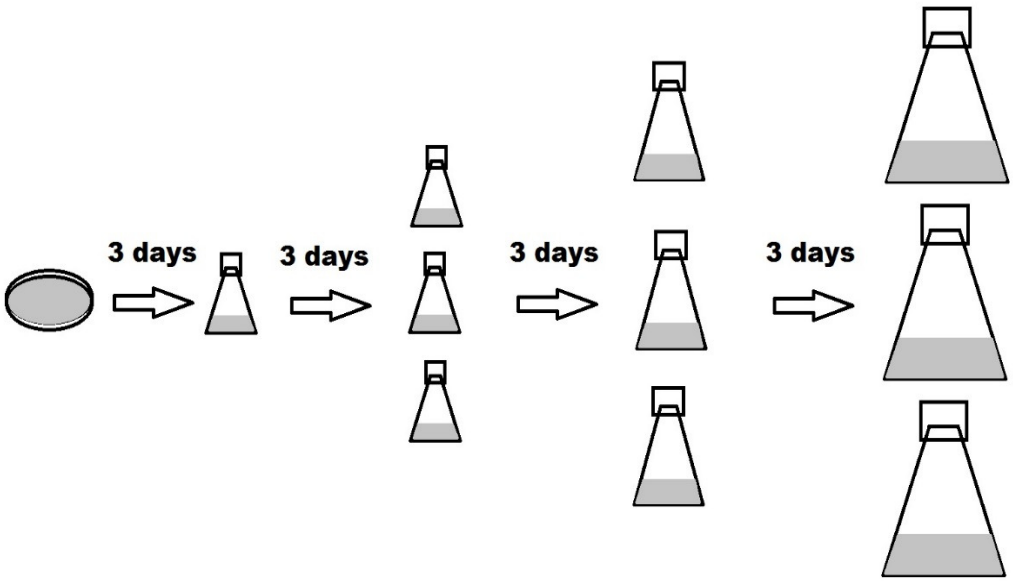

Figure 2-2: *D. discoideum* axenic growth for large-scale

When the cells reach a density of of 1×10^7 -2×10^7 cells/ml, they are ready to be harvested by centrifugation. Wash with MES buffer and resuspend in lysis buffer with protease inhibitor. Slowly drip small cell drops into the liquid nitrogen. The cells should be frozen into a pile of perfect spheres and stored at -80°C.

2.2.2 Myosin Motor Domain Purification

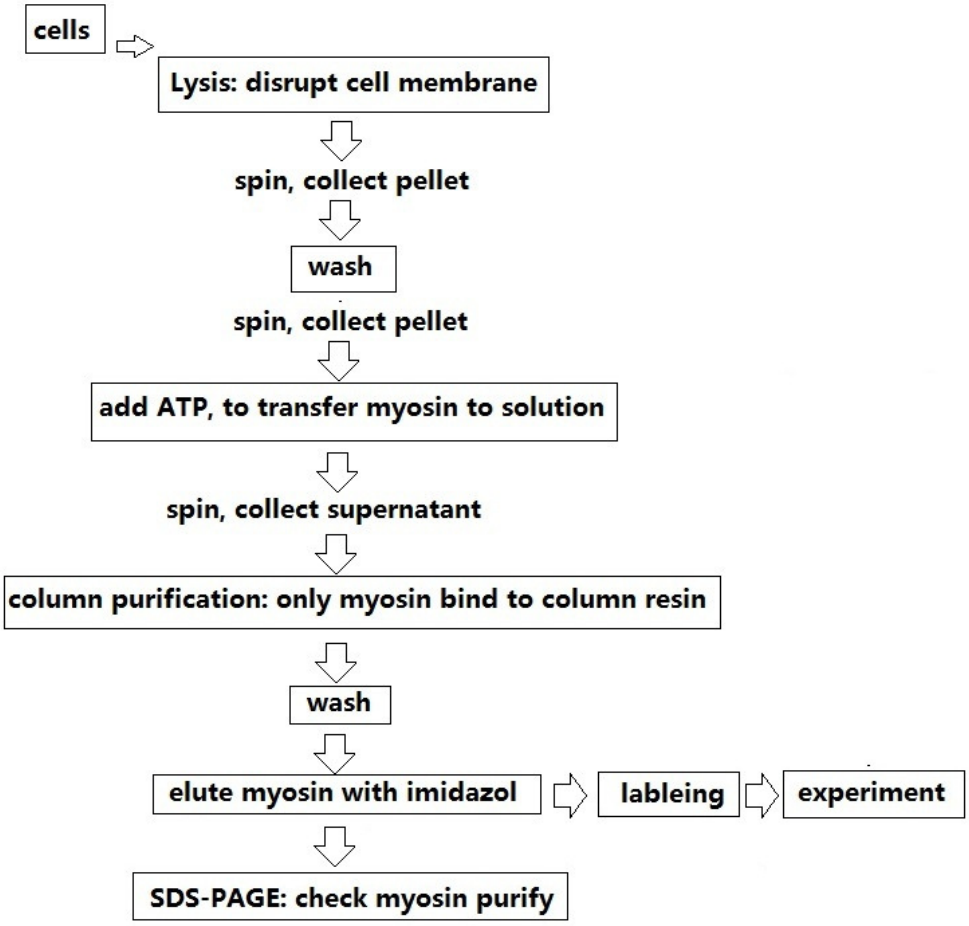

Figure 2-3: Myosin S1dC purification from frozen cells

Myosin preparation starting from frozen cells used the basic procedure established by Manstein & Hunt (10) with the following modification: Talon affinity resin was used rather than Ni^{2+}-NTA, and the S1dC myosin was eluted in batches of buffer with a step gradient of imidazole (100 mM, 200 mM, 300 mM) rather than a continuous gradient. The eluted S1dC was then washed with experimental buffer (20mM MOPS (3-(N-morpholino)propanesulfonic acid), 50mM potassium chloride, pH=7.3) at 4°C using Amicon filters (30 kDa cutoff). Usually 20ul samples from each step should be saved for running a gel, one gel picture was attached to show the purification (Figure 2-4).

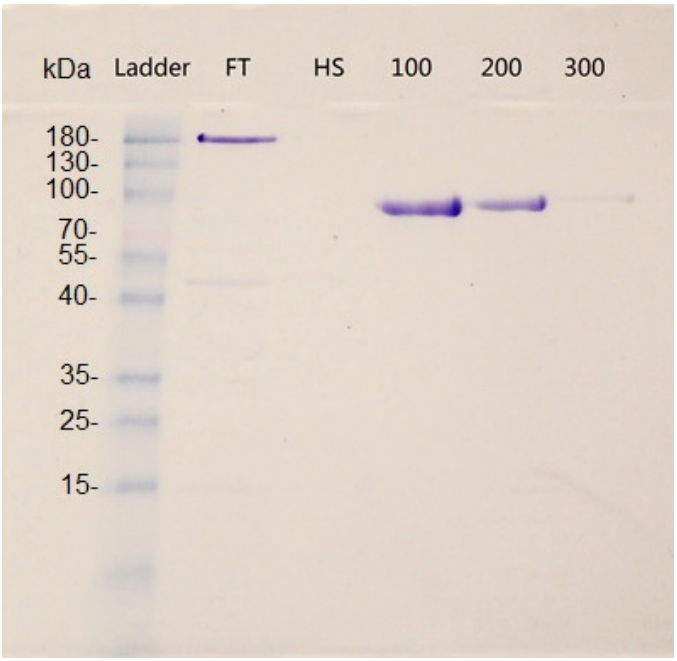

Figure 2-4: Gel picture for cellular myosin preparation. From left to right, prestained protein ladder, flow through (FT), high salt (HS), elution with a step gradient of imidazole 100 mM, 200 mM, and 300 mM

2.2.3 Myosin Motor Domain Labeling

For FRET measurements protein was labeled in two steps (11). First, 50 mM myosin was incubated with 25 mM donor (1,5-IAEDANS, 5-((((2-Iodoacetyl)amino)ethyl)amino) Naphthalene-1-Sulfonic Acid) for 12 hours on ice, then protein was diluted to 25 mM and incubated with 100 mM acceptor (Dabcyl, SE, 4-((4-(dimethylamino)phenyl)azo)benzoic Acid). After final labeling step, unreacted label was removed with Amicon filter and labeled myosin was centrifuged at 30,000 rpm (F40L rotor) for 1 hour to remove possible aggregates and dead myosin before experiments.

The concentration of unlabeled myosin was determined spectrophotometrically at 280 nm using an extinction coefficient of A280nm = 0.69 $(mg/mL)^{-1}$ cm^{-1}. The concentration of the labeled myosin was determined by Bradford assay (12).

2.3 Myosin Purification from Skeletal Muscle

The solubility of a protein in salts is determined by its charge and hydrophobicity. Myosin is highly soluble in high salt solutions, whereas actin is more soluble in low salt. This difference in salt solubility can, therefore, provide a convenient first step in fractionating the two proteins from skeletal muscle cells(13, 14).

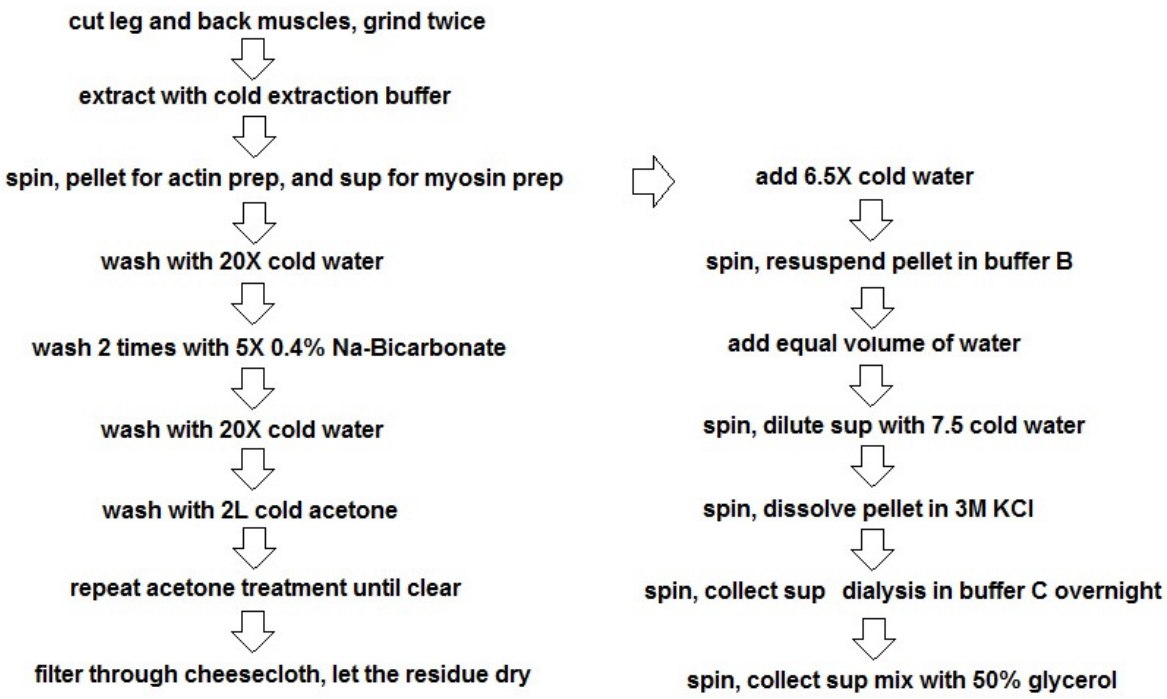

Figure 2-5: Skeletal myosin and actin preparation from rabbit muscle

Purification started from grinding the rabbit leg and back muscle twice in meat grinder. Extract the high salt-soluble proteins into the soluble (supernatant) fraction during centrifugation. Those that are more soluble in low salt will remain in the insoluble (pellet) fraction. It is then possible to achieve further purification of the high salt-soluble proteins by then lowering the concentration of salt in the solution by adding water. This will cause myosin and other high salt-soluble proteins to now become insoluble and precipitate out of the low salt solution.

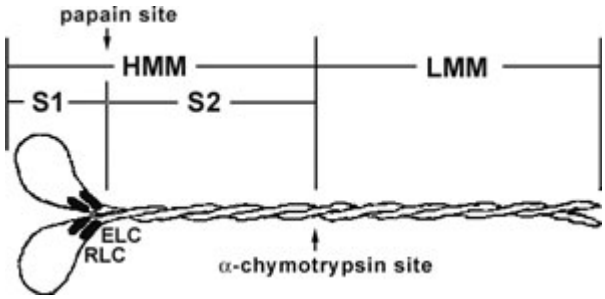

Figure 2-6: Diagrammatic representation of the myosin subfragments

Rabbit skeletal myosin purified from previous steps was a hexameric protein consisting of two heavy chains and two light chains, see Figure 2-6. The full length myosin protein has been purified with its essential light chains (ELC) and regulatory light chains (RLC).

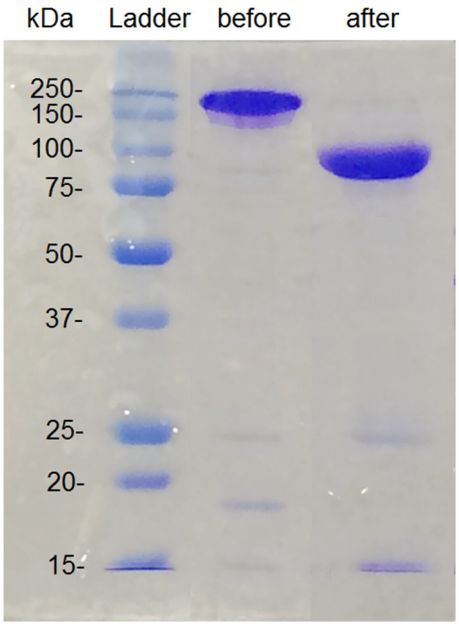

Figure 2-7: Gel picture for rabbit skeletal myosin preparation. From left to right, prestained protein ladder, rabbit skeletal myosin before digestion, rabbit skeletal myosin after digestion

Myosin can be proteolytically cleaved into heavy meromyosin (HMM) and light meromyosin (LMM) by adding 30 ug/mL α-chymotrypsin and quenched by 2mM PMSF in 15 minutes. We have HMM after digestion with chymotrypsin. So we digest, quench digestion with PMSF, spin and collect soluble HMM (15).

2.4 Actin Purification and Labeling

Actin was prepared from rabbit back and leg muscles as described(16). First step of crude actin purification occurred during preparation of acetone powder – particularly during bicarbonate washes. Second step of actin preparations was obtained by cycles of polymerization-depolymerization using potassium chloride.

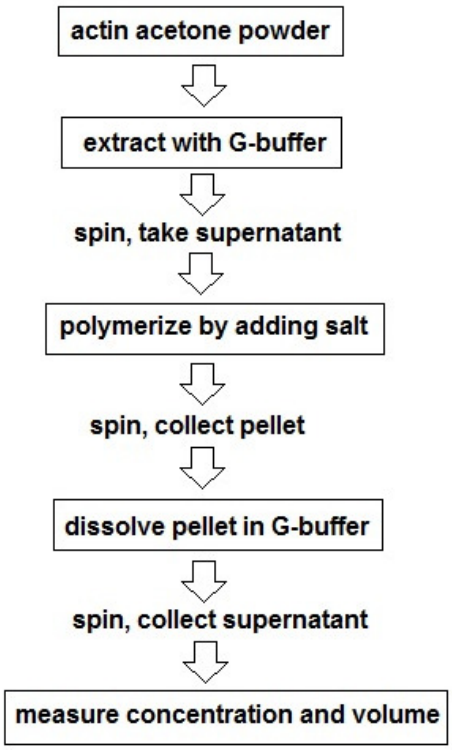

Figure 2-8: Actin preparation from acetone powder

Acetone-dried powder of rabbit skeletal muscles was prepared by the method of Feuer et al. The muscle was ground in a meat grinder and extracted for 10 minutes with 3 volumes of cold Guba-Straub buffer. (Guba-Straub solution 0.3M KCl, 0.15 M potassium phosphate buffer, pH 6.5). Centrifuge at 4,000 rpm 10 minutes, and wash pellets with 20 volumes of cold dH_2O and twice with 5 volumes 0.4% Na-bicarbonate solution. It was then quickly washed twice with 5 vol. deionized water, dehydrated by washing several times with acetone, air-dried overnight and stored in a freezer. This kind of muscle powder will be further referred to as the “acetone-dried” powder.

Further actin preparations from the acetone-dried powders started from extraction with 20 volumes G-buffer (5 mM Tris, 0.2 mM $CaCl_2$, 0.5 mM ATP, pH 7.5) for 30 min on ice (17). Spin down insoluble material in the table top centrifuge at max speed. Combine supernatants and polymerize actin for about 1 hour at room temperature by adding 2mM MgCl2 and 50mM KCl. F-actin was collected by centrifugation for 1 hour at 60,000 rpm (18). Homogenize pellet in G-buffer for about 5 min. Final preparations were clarified by 1-hour centrifugation at 60,000 rpm. Collect supernatant and measure concentration of G-actin. Concentration of unlabeled G-actin was determined spectrophotometrically assuming the extinction coefficient $\varepsilon_{290nm} = 0.63\ (mg/ml)^{-1}cm^{-1}$ (19). Monomeric actin, obtained by this method, should be stored on ice, up to 10 days. The structure of actin is preserved within this period of time. SDS-page gel was carried out to assess the progress of purification (Figure 2-9).

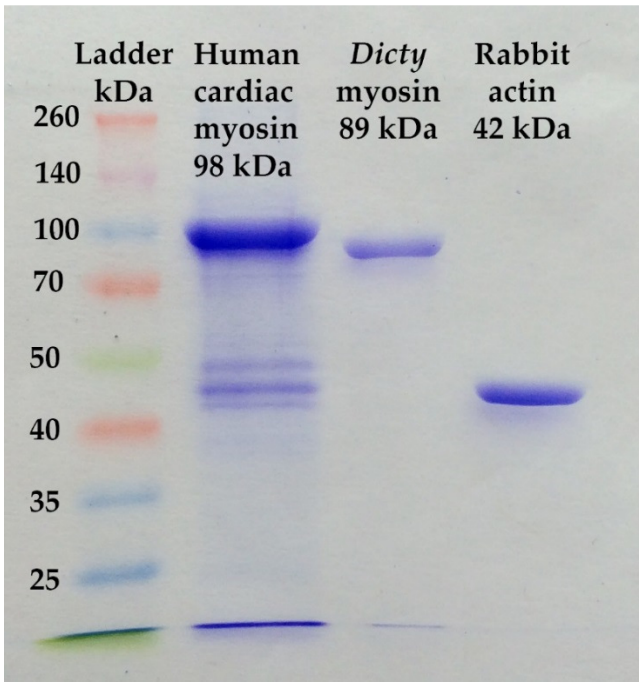

Figure 2-9: Gel picture for rabbit skeletal actin.
From left to right, prestained protein ladder, human cardiac myosin, *Dicty* myosin, and Rabbit actin

Actin was polymerized by adding 2mM MgCl2 and 50mM KCl for about 1 hour at room temperature. F-actin was labeled with pyrene iodoacetamide or TEMPO

maleimide (6:1 label:actin molar ratio). Spin down insoluble material in the table top centrifuge at max speed at 4ºC for 15 minutes. Centrifuged labelled F-actin for 1 hour at 60,000 rpm (T-865) at 4ºC. Discarded supernatant, homogenized pellet in G-buffer for about 5 min, cleaned from the excess label. Repolymerized to F-actin by adding salt, spin down 1 hour at 60,000 rpm (T-865) at 4ºC, dissolved pellet in F-buffer, stabilized with phalloidin at a molar ratio of 1:1 (phalloidin:actin), and dialyzed for two days at T=4ºC against the experimental buffer. Concentration of labeled G-actin and labeling efficiency were determined spectroscopically using the following expressions: $[\text{G-actin}]=(A_{290nm}-(A_{344nm}\cdot 0.127))/26{,}600\ M^{-1}$ and $[\text{pyrene}]=A_{344nm}/22{,}000\ M^{-1}$ (20).

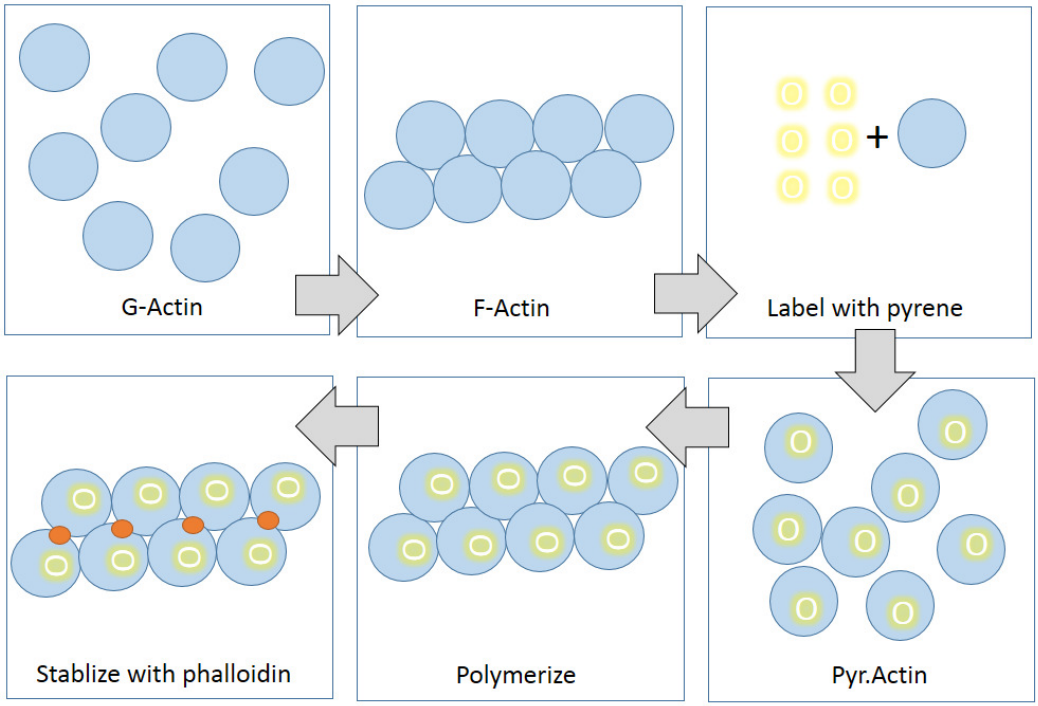

Figure 2-10: An illustration of Actin labelling

CHAPTER 3: RESEARCH METHODOLOGY

3.1 SDS-PAGE

Electrophoresis is a method to separating macromolecules in an electric field. One useful tool is called Sodium dodecyl sulfate polyacrylamide gel electrophoresis (SDS-PAGE) which employs a discontinuous polyacrylamide gel as a restraining medium and sodium dodecyl sulfate (SDS) to denature the proteins. In a gel of uniform density, the relative migration distance of a protein is negatively proportional to the log of its mass. The mass of unknown proteins can be estimated if knowns are run and plotted simultaneously(21). SDS-PAGE can be used to estimate protein molecular mass, to determine the purity of major protein in an abundant sample, and to determine the distribution of proteins among fractions.

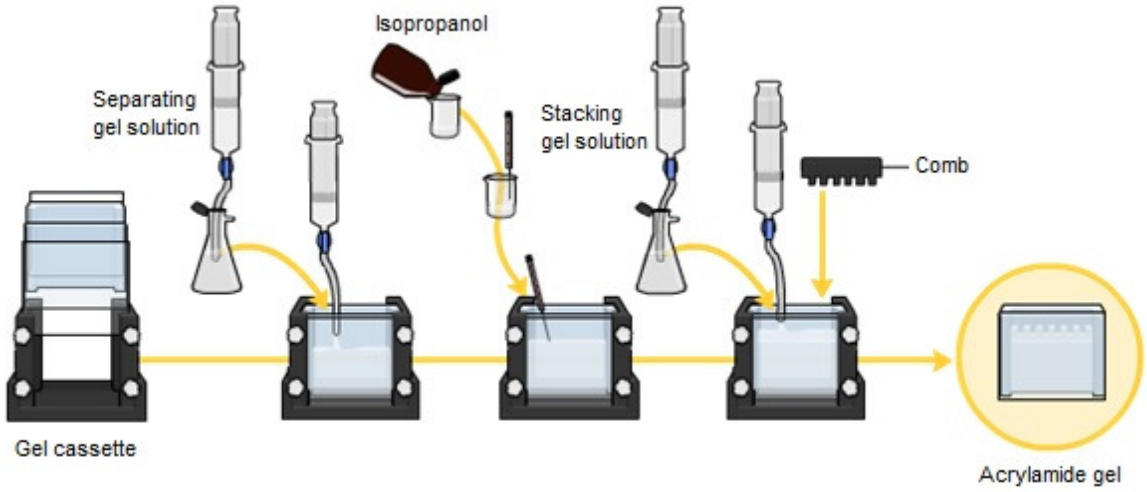

Figure 3-1: SDS-PAGE gel preparation

The SDS-PAGE gels were prepared between two glass plates in a gel cassette, with a comb inserted at the top to create the sample wells, as shown in Figure 3-1. We used a "mini-gel" system, with 3 1/4" x 4" gel cassettes. Gels including separating gel (lower

part) and stacking gel (upper part) were polymerized in two steps. The separating gel consisted of 10-15% acrylamide/bisacrylamide (37.5:1), depending on the size of the analyzed proteins, 375 mM Tris base, pH 8.8, 0.1% SDS, with 0.1% Ammonium Persulfate (APS) and 0.04% N,N,N',N'- tetramethylethylenediamine (TEMED) to start polymerization. At the meantime, the stacking gel consisted of 5% acrylamide/N,N'-methylene-bis-acrylamide (37.5:1), 125 mM Tris base, pH 6.8, 0.1% SDS, with 0.1% APS and 0.1% TEMED to start polymerization. A layer of isopropanol (1 ml) was added between these two steps to remove bubble and maintain absolute horizontal surface. After polymerization, the gels could be wrapped with wet napkins and stored at 4°C up to two weeks.

The comb should be removed when the gel was ready for electrophoresis. Apparatus was setup as shown in Figure 3-2. Separation of the proteins was performed by gel electrophoresis under reducing and denaturing conditions. Therefore, sample proteins were prepared with Laemmli buffer (2% SDS, 10% glycerol, 100 mM DTT, 0.01% bromophenol blue, 10 mM Tris-HCl, pH 6.8) plus 5% β-mercaptoethanol, boiled 5 minutes, and loaded into wells together with a standard ladder on the side. We got the best results if 20 µl of a 2 mg/ml final concentration of denatured protein was loaded per sample well of a typical mini-gel. 10 µl of ladder would be enough for a reference.

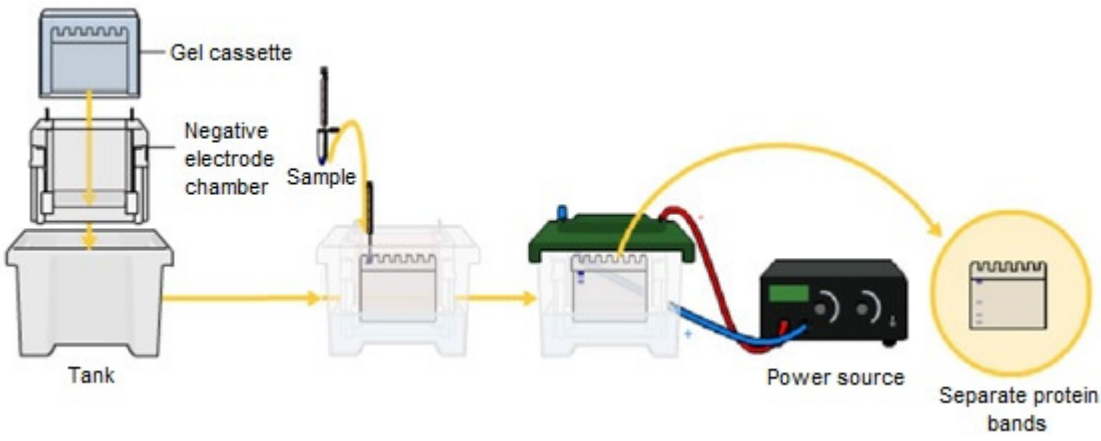

Figure 3-2: An illustration of SDS-PAGE apparatus setup

The electrophoresis was run for one to two hours at a constant current of 30 mA with the electrophoresis running buffer containing 25 mM Tris base, 192 mM glycine and 0.1% SDS. Stain the gel one hour in the Coomassie blue stain solution, containing 0.1% Coomassie Blue R-250, 41.7% methanol, 16.7% acetic acid and 41.7% Water, until the gel is a uniform blue. Destain for 12 - 24 hours in 8.7% acetic acid, 17.4% methanol, 17.4% isopropanol and 56.5% water. Store the gel in water after destaining.

3.2 ATPase Assays

Basal and actin-activated myosin ATPase activity was measured at $T = 25°C$ in the experimental buffer with 5 m*M* ATP and 5 m*M* $MgCl_2$ (substitute with $MnCl_2$, or $CaCl_2$ in Chapter IV) in the presence and absence of actin, by the liberation of inorganic phosphate (22). Myosin or actomyosin were mixed with ATP and aliquots were collected in equal time intervals and analyzed for phosphate by adding ammonium molybdate–malachite green solution and quenching the reaction with sodium citrate, as shown in Figure 3-3. All added solutions contained 1*N* HCl for stable color formation. The absorption of the resulting mix at 620 nm is proportional to phosphate concentration.

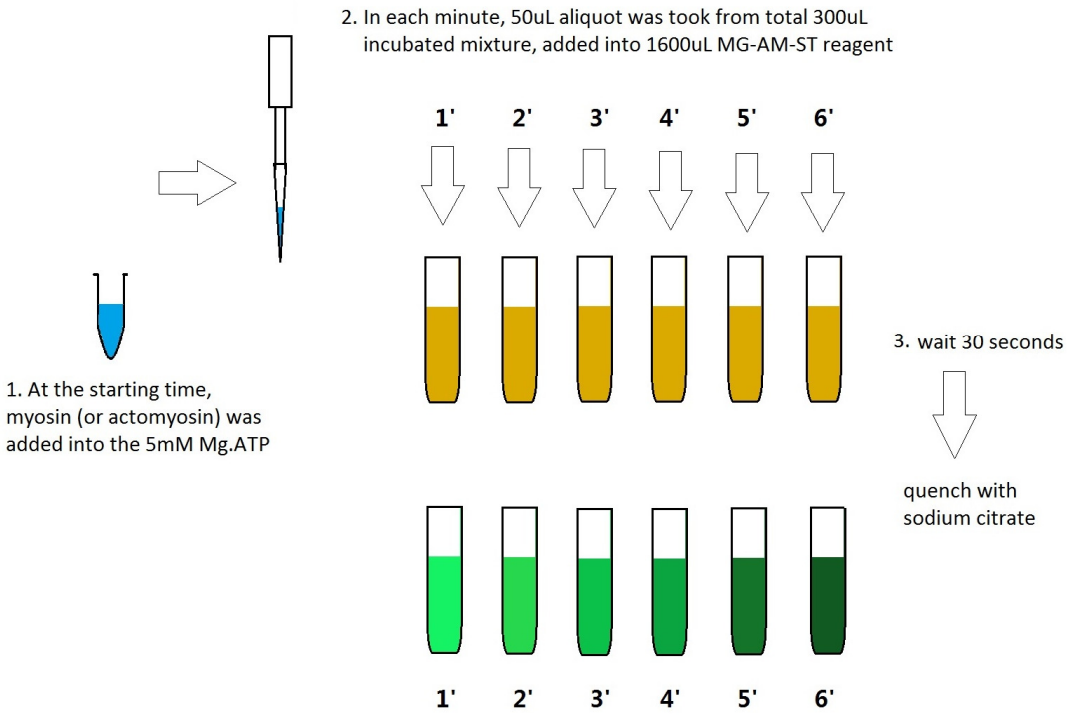

Figure 3-3: Stead-state ATPase operating procedures

To quantify phosphate production in the hydrolysis reaction, the obtained myosin and actomyosin data were compared with the data of the same reaction, performed with the phosphate standard of known concentration, Figure 3-4.

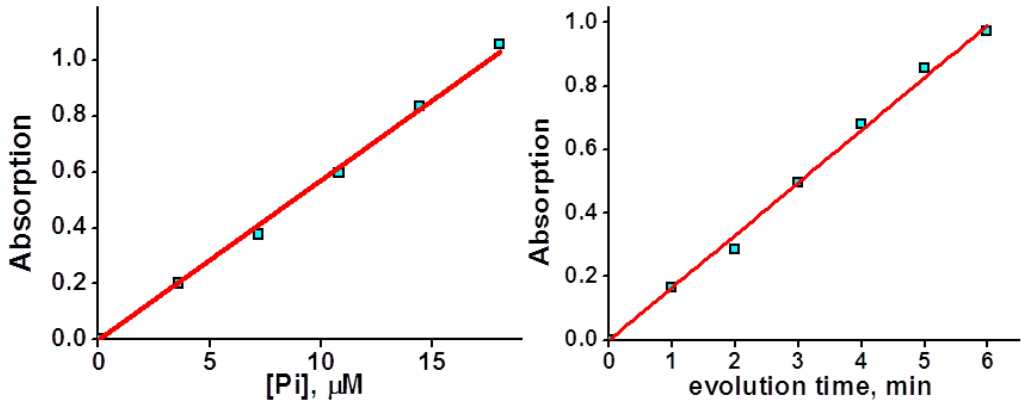

Figure 3-4: Basal myosin ATPase activity measurement

Left, phosphate absorption. Phosphate aliquots of known concentration added to the reagent consisted of 1% of ammonium molybdate, 0.0325% of malakhite green, and 2% of Sterox in 1N HCl. 34% sodium citrate in 1N HCl added to the mixture in 30 seconds to stabilize color formation. Absorption at 620 nm

recorded in 10 minutes after citrate addition. Right, time resolved phosphate production by myosin ATPase upon mixing with ATP. Myosin was mixed with ATP (T=25°C) and 50uL aliquots were taken each minute and added to the reagent. Sodium citrate was added in 30 seconds and absorption of the mixture was read after 10 minutes.

Myosin basal ATPase activity was determined by normalization of the data on the concentrations of phosphate and myosin to obtain the rate of phosphate production per myosin head per second. To determine the maximum velocity of the actomyosin ATPase, the data were fitted to the modified Briggs-Haldane equation $v = V_{basal} + V_{max}[actin]/(K_m + [actin])$, where v is the rate of the ATPase in the presence of actin, V_{basal} is the rate of myosin ATPase without actin, V_{max} is the rate of myosin ATPase at infinite actin concentration, and K_m is the Michaelis constant. The modification of the Brigg-Haldane equation accounts for possible basal ATPase activity of myosin in the presence of actin(11).

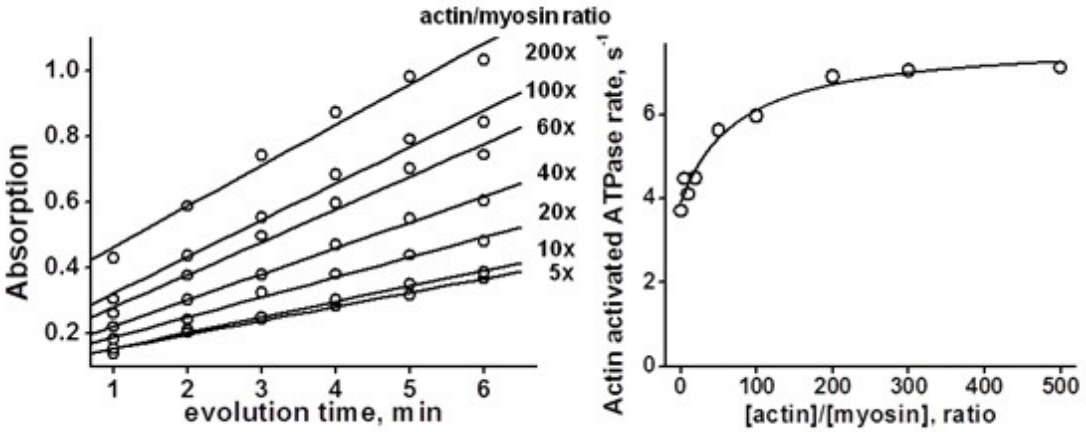

Figure 3-5: Measurement of the rate of actin activated myosin ATPase. Left, time resolved phosphate production by myosin, premixed with actin at different ratios, and then mixed with ATP. Right, observed rates of actin activated myosin ATPase, fitted to the modified Briggs-Haldane equation.

3.3 Transient Fluorescence

Transient myosin intrinsic fluorescence and pyrene actin fluorescence was measured with Bio-Logic SFM-300 stopped-flow transient fluorimeter, equipped with FC-15 cuvette. The stopped-flow transient fluorimeter is a rapid mixing transient

kinetic technique in which the aging of a reaction can be followed optically on a millisecond timescale. The reagents are in different syringes that are pushed by a computer-driven motor simultaneously. The mixing unit dead time is 2.4 milliseconds. All experiments were done at T = 20ºC. Two or three syringes (one or two mixers) were used depending on the experiment.

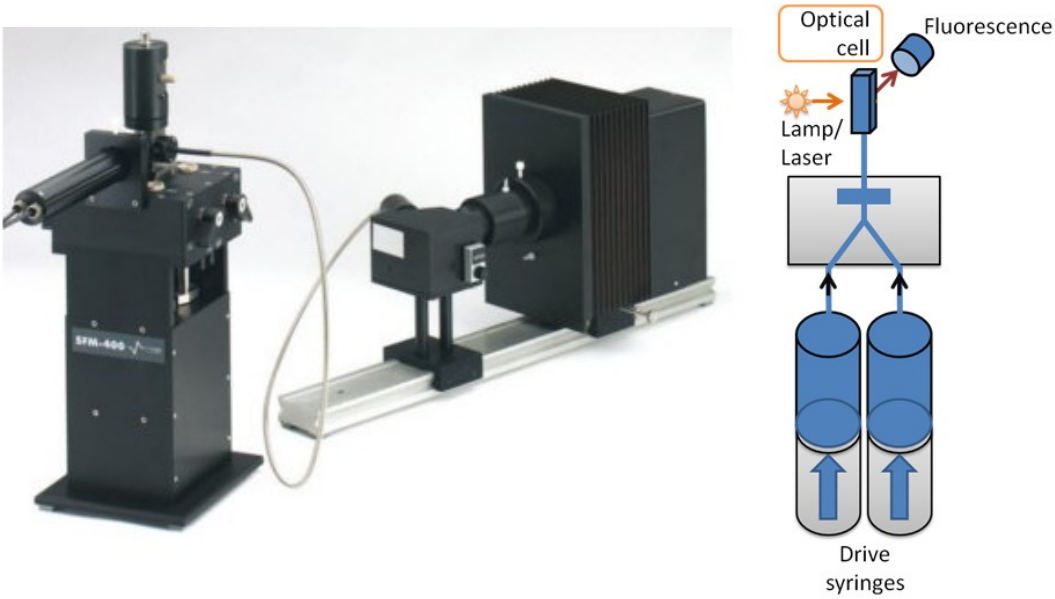

Figure 3-6: Bio-Logic SFM-300 stopped flow transient fluorimeter

The intrinsic tryptophan fluorescence signals were monitored to follow the conformational changes within the myosin head, and the fluorescence intensity change of pyrene labeled actin reflected binding or dissociation from the myosin head. Myosin intrinsic fluorescence was excited by mercury-xenon lamp at 302 nm, and detected using 320 nm cutoff filter. Pyrene fluorescence was excited at 365 nm and detected using 420 nm cutoff filter. Multiple traces were usually acquired and averaged to improve signal to noise ratio. Maximum number of points was acquired in all experiments (8000 points) and then experimental points were selected according to the logarithmic scale to reduce fitting time.

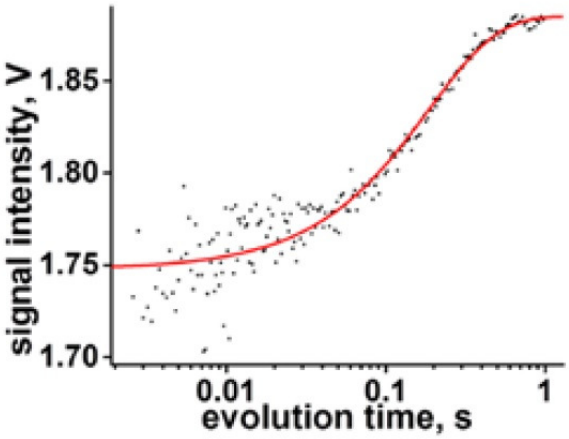

Figure 3-7: Intrinsic fluorescence transient after rapid mixing of 0.5 μM myosin and 18 μM ATP, Line, a single-exponential fit.

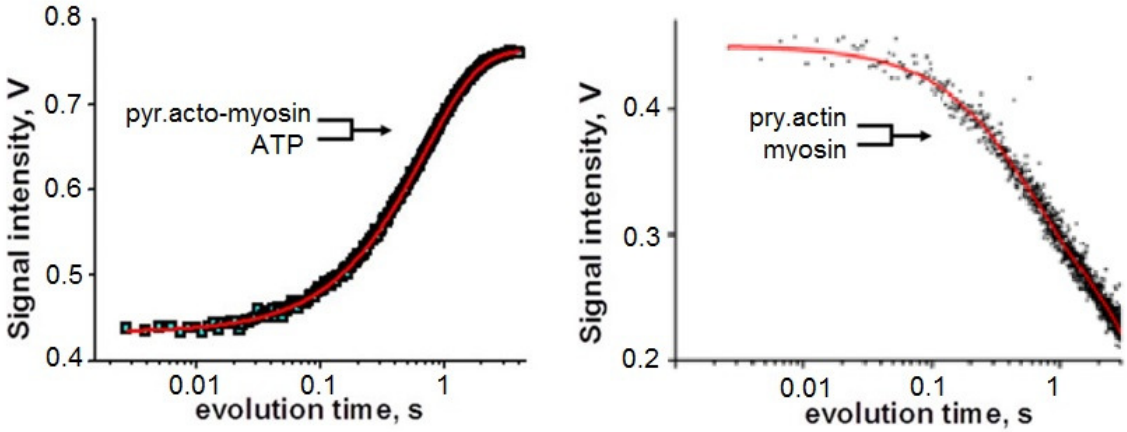

Figure 3-8: Transients of pyrene.actin fluoresence. Left: ATP-induced actomyosin dissociation, pyrene fluorescence transient after rapid mixing of 50 mM ATP and 0.15 mM pyrene.acto-myosin, fitted with two exponents. Right, actomyosin rigor binding, 0.15 μM pyrene actin rapidly mixed with 0.9 μM myosin, fitted with a single-exponential.

3.4 Fluorescence Resonance Energy Transfer (FRET)

Transient time resolved FRET (TR^2FRET) was measured with the home built transient fluorimeter, based on Applied Photophysics SX-18 stopped flow unit, equipped with passively Q-switched microchip YAG laser, photomultiplier, and fast digitizer (Figure 3-9). Dead time of the mixing unit is 2.6 ms. All experiments were done at 20^{o}C.

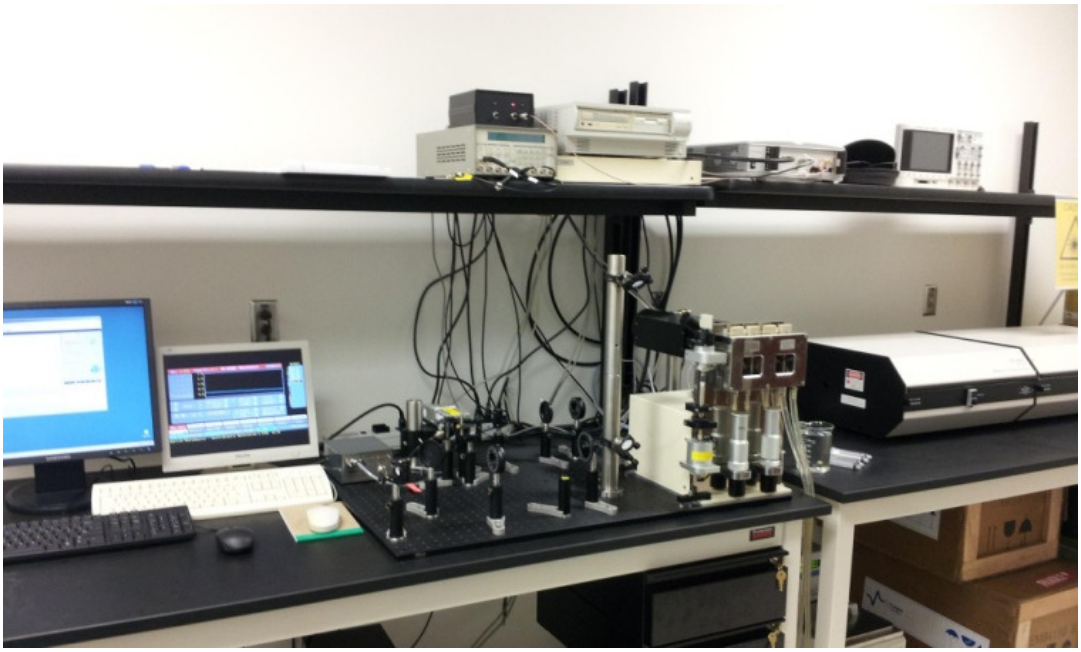

Figure 3-9: Transient time resolved FRET fluorimeter

Fluorescence of IAEDANS-myosin was excited with the third harmonic (355 nm) of a passively Q-switched microchip yttrium aluminum garnet laser (SNV-20F-100, Teem Photonics), operated at a pulse repetition frequency of 20 kHz. To avoid anisotropy effects, fluorescence was passed through a polarizer oriented at the magic angle.

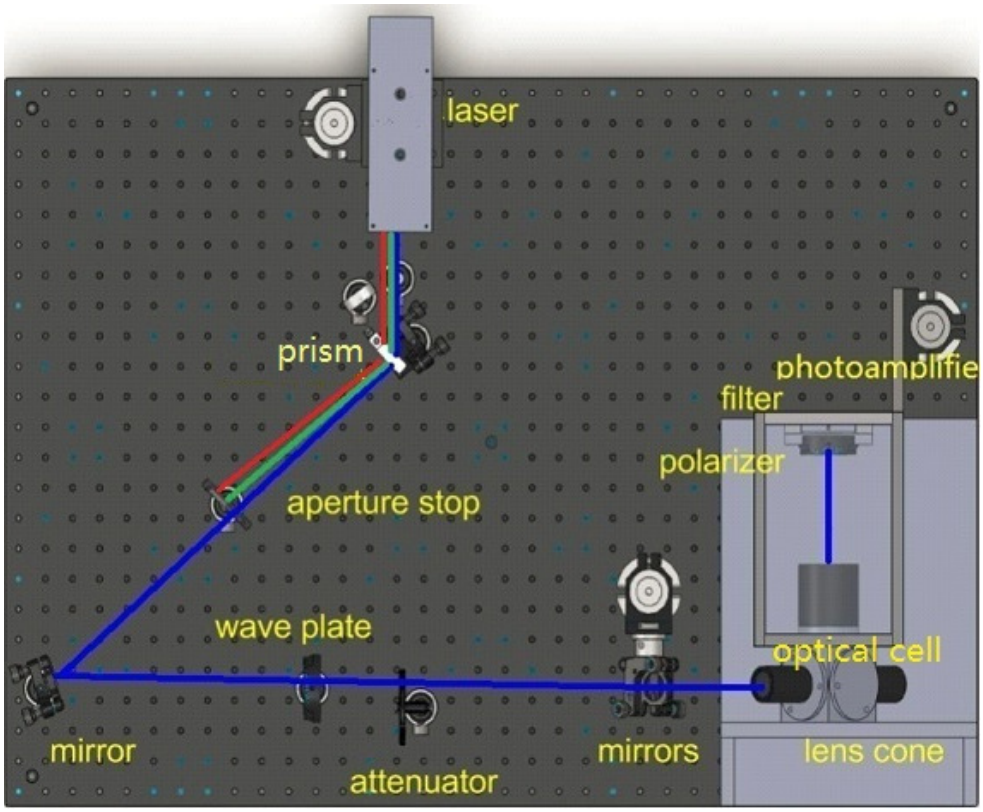

Figure 3-10: Optical pathway diagram for transient time resolved FRET fluorimeter

Fluorescence signals were detected after every laser pulse with a photomultiplier module (H6779-20, Hamamatsu) and acquired with a transient digitizer (Acqiris DC252, Agilent) with time resolution of 0.125 ns (8 GS⁄s), as shown in Figure 3-11.

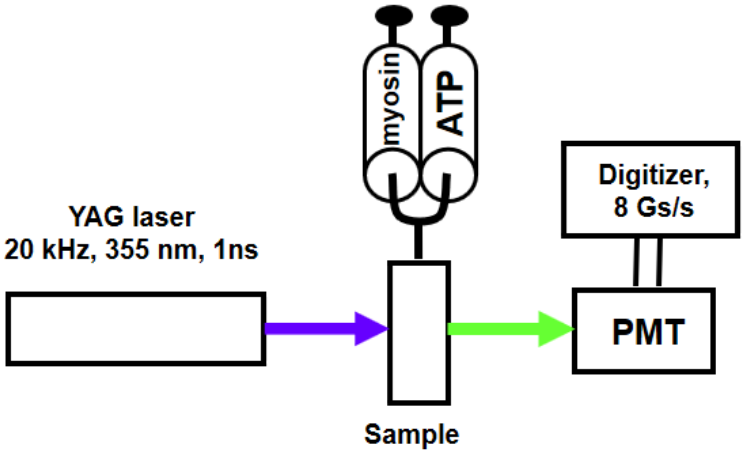

Figure 3-11: An illustration of transient time resolved FRET fluorimeter

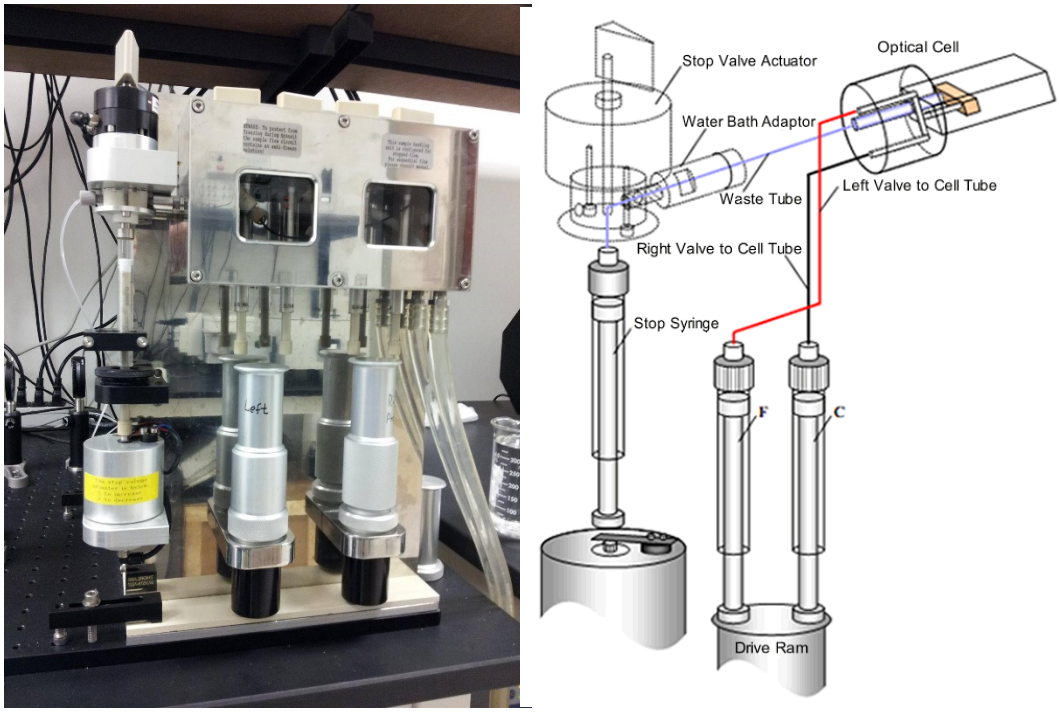

Figure 3-12: Stopped-flow apparatus for transient time resolved FRET fluorimeter

To obtain FRET data, a stopped-flow apparatus was attached to the fluorometer to measure transient kinetics of the myosin–ATP reaction. FRET pair labeled myosin was rapidly mixed with ATP solution, and donor fluorescence was acquired after each laser pulse with the picosecond resolution. Multiple traces were usually acquired and averaged to increase signal to noise ratio.

In FRET experiment we expect to observe the waveforms of the fluorescence of donor-acceptor labeled myosin in two structural states, M* and M**, and the fluorescence of donor-only labeled myosin. The acceptor (Dabcyl) is not fluorescent, and we do not expect to detect fluorescence from the acceptor. Therefore, the waveform of observed transient fluorescence at each time point was fitted as a sum of three components, convoluted with the instrument response function (Figure 3-14, determined from the light scatter).

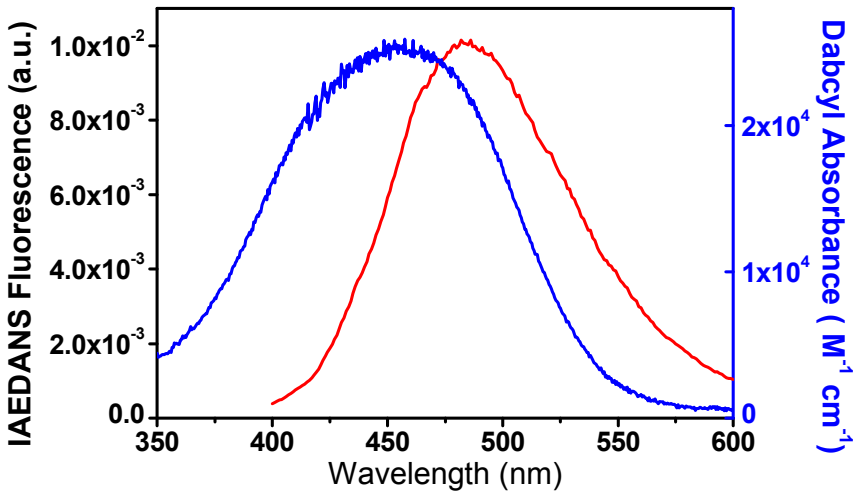

Figure 3-13: Spectral overlap of donor emission (blue) and acceptor absorption (red) gives FRET efficiency, characterized with R_0, the distance of 50% FRET effect.

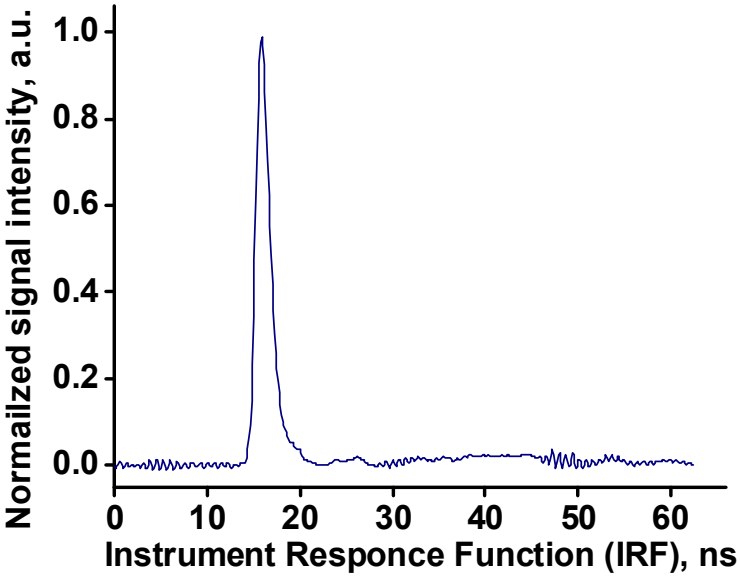

Figure 3-14: Instrument Response Function (IRF) obtained from light scatter

The parameters of donor fluorescence were determined in the separate experiment with donor-only labeled myosin, according to Eq. (3.1),

$$F_D(t) = \sum_{i=1}^{2} A_i \exp(-t/\tau_{Di}), \tag{3.1}$$

where τ_{Di} are donor-only fluorescence lifetimes.

The interprobe distance and distance distribution $\rho(r)$ in the M* state were determined in the experiment with donor-acceptor labeled myosin without ATP,

according to the Eq. (3.2). The parameters of the donor fluorescence, determined in the previous experiment, were kept fixed.

$$F_{DA}(t) = \int_0^{+\infty} \rho(r) \cdot \sum_{i-1}^{2} A_i \exp\left\{\left(-\frac{t}{\tau_D}\right) \cdot \left(1 + \left[\frac{R_0}{r}\right]^6\right)\right\} dr, \quad (3.2)$$

where R_0 = 4 nm is the Förster distance for IAEDANS-Dabcyl pair (8) and $\rho(r)$ is a probability density function to account for interprobe distance distribution. We used Gaussian distribution as a probability density function.

$$\rho(r) = \sigma^{1}(2\pi)^{-1/2} \exp(-[(r-R)/\sigma]^2/2), \quad (3.3)$$

where σ is the standard deviation, determining the interprobe distance distribution, and R is the position of the distribution maximum.

The mole fraction of the M** state, and corresponding interprobe distance and distance distribution were determined from the experiment when myosin was rapidly mixed with ATP. Experimental data were fitted to the Eq. (3.4), with all previously determined parameters fixed.

$$F_{total}(t) = X \cdot F_D(t) + X^* \cdot F_{DA^*}(t) + X^{**} \cdot F_{DA^{**}}(t), \quad X + X^* + X^{**} = 1, \quad (3.4)$$

In this equation, X without and with superscripts are the mole fractions of donor-donor labeled myosin (X), and donor-acceptor labeled myosin in M* and M** structural states.

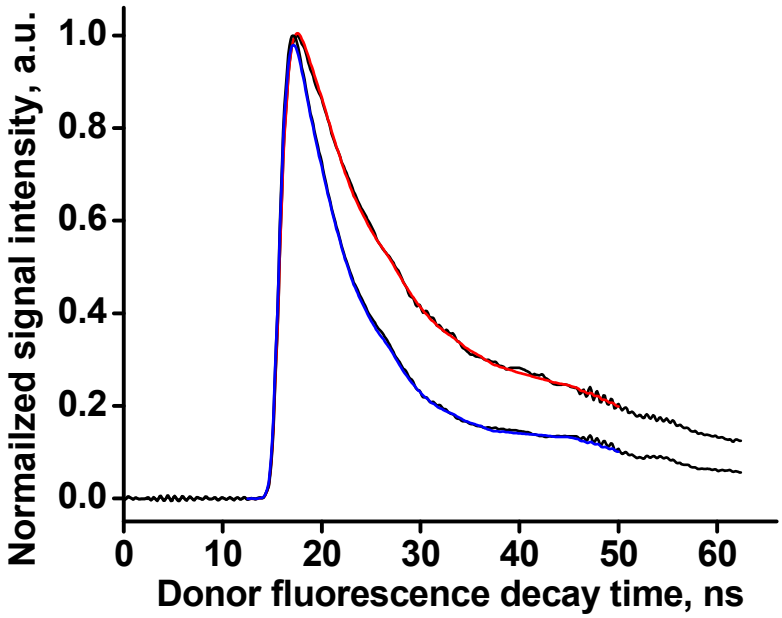

Figure 3-15: Donor fluorescence fitted with two-exponential decay fuction.
Red: donor-only labeled myosin; blue: donor-acceptor labeled myosin.

Analysis of transient time-resolved fluorescence data was performed using software package FargoFit, designed by I. Negrashov, that executes global least-square fitting of multiple time-resolved fluorescence waveforms using different kinetic models with ability to link fitting parameters between waveforms.

CHAPTER 4: EFFECT OF DIVALENT METAL CATION ON ACTOMYOSIN ATPASE KINETCS

4.1 Introduction

Myosin changes conformation upon ligand binding, producing the recovery stroke (interaction with ATP) and then the power stroke, upon interaction with actin. It was shown previously that the cross-bridge kinetics can be directly modulated by altering a nucleoside triphosphate (23-26), which apparently affects position of the triphosphate within myosin active site. Metal cation, coordinating β and γ phosphates of a nucleotide at the active site, should modulate myosin-nucleotide interaction in even larger extent, affecting kinetic steps of myosin ATPase. The goal of this work was to determine if the kinetics of myosin and actomyosin ATPase cycle can be modulated using different metal cations, complexed with ATP. Direct modulation of myosin and actomyosin kinetics is an attractive approach in myopathies treatment. Fine tuning of myosin kinetics may increase muscle performance and muscle power output in a diseased muscle.

It is known that calcium and manganese support myosin and cross-bridge ATPase activity (27-30), as well as natural ligand Mg.ATP, and the rate of basal myosin ATPase depends on metal cation, complexed with ATP. Intrinsic fluorescence of myosin, rapidly mixed with Mn.ATP, exhibits apparent rapid destabilization of the post-recovery stroke state (M** state) (31), suggesting increased rate of the reverse recovery stroke and phosphate release, which therefore can be responsible for observed increased rate of myosin ATPase activity. All these data suggest that myosin is not a specific enzyme and interacts with nucleotide, complexed with different divalent metal cations.

This allows systematic study of myosin kinetic response on different metal cations, placed right in the center of the hydrolysis reaction. In this work we provide detailed study and rational clarification of the effect of metal cation on myosin and actomyosin ATPase activity.

4.2 Experimental

4.2.1 Sample Preparation

Actin was prepared from rabbit back and leg muscles as described previously in Chapter 2. Both labeled and unlabeled actin were included in this study. Actin was labeled with pyrene (8:1 label:actin molar ratio) and stabilized with phalloidin (1.1:1 phalloidin:actin molar ratio). Concentration of unlabeled actin was determined spectrophotometrically assuming extinction coefficient $A_{290\ nm} = 0.63\ (mg/mL)^{-1}cm^{-1}$. Concentration of labeled actin was determined with the Bradford assay (BioRad).

A639C:K498C mutant of *D. discoideum* myosin motor domain was constructed and purified as described previously in Chapter 2. For FRET measurements, myosin was labeled with donor (IAEDANS) and with acceptor (DABCYL) in two steps. Concentration of unlabeled myosin was determined spectrophotometrically assuming extinction coefficient $A280nm = 0.69\ (mg/mL)^{-1}cm^{-1}$. Concentration of labeled myosin was determined with Bradford assay (BioRad).

The experimental buffer contained 20 m*M* MOPS pH 7.5, 50 m*M* KCl, with 3m*M* metal cation ($MgCl_2$, or $MnCl_2$, or $CaCl_2$).

4.2.2 ATPase Assays

Myosin ATPase activity was measured at $T = 25°C$ in the experimental buffer with 5 m*M* ATP and 5 m*M* metal cation ($MgCl_2$, or $MnCl_2$, or $CaCl_2$) in the presence and absence of actin, by the liberation of inorganic phosphate as described previously in Chapter 3.

Transient time resolved FRET was measured with the home built transient fluorimeter, based on Applied Photophysics SX-18 stopped flow unit, equipped with passively Q-switched microchip YAG laser (SNV-20F-100, Teem Photonics, 355 nm, 20 kHz), photomultiplier (H6779-20, Hamamatsu), and fast digitizer (Acqiris DC252, Agilent). Dead time of the mixing unit is 2.6 ms. All experiments were done at T = 20^{o}C. FRET pair labeled myosin was rapidly mixed with metal.ATP solution, and donor fluorescence was acquired after each laser pulse with the picosecond resolution. Multiple traces were usually acquired and averaged to increase signal to noise ratio. The analysis of transient time-resolved luminescence data was performed using software package FargoFit, executing global least-square fitting of multiple time-resolved luminescence waveforms using different models with ability to link fitting parameters between waveforms. The analysis of the donor lifetime in terms of myosin structural conformations M* and M**, pre- and post-recovery stroke states, was described in Chapter 3 research methodology.

Transient myosin intrinsic fluorescence and pyrene actin fluorescence was measured with Bio-Logic SFM-300 stopped flow transient fluorimeter, equipped with FC-15 cuvette. The mixing unit dead time is 2.4 ms. All experiments were done at T = 20^{o}C. Two or three syringes (one or two mixers) were used depending on the experiment. Myosin intrinsic fluorescence was excited by mercury-xenon lamp at 302 nm, and detected using 320 nm cutoff filter. Pyrene fluorescence was excited at 365 nm and detected using 420 nm cutoff filter. Multiple traces were usually acquired and averaged to improve signal to noise ratio. Maximum number of points was acquired in all experiments (8000 points) and then experimental points were selected according to the logarithmic scale to reduce fitting time.

4.2.3 Analysis of Transients

Transients of myosin conformational change were measured by rapid mixing of myosin (0.8 μ*M* in intrinsic fluorescence, and 10 μ*M* in FRET, syringe concentrations) and ATP of variable concentrations. In the result, the rate constants $K_1K_2k_{+3}$ ($K_1K_2k_{+3}\cdot[\mathrm{ATP}]=k_{+3}$) and k_{-3} for myosin-Mg.ATP transients, and k_{+3}, k_{-3}, k_{+4}, $k_{+6}K_7$ for myosin-Mn.ATP and myosin-Ca.ATP transients were determined. Kinetics of myosin intrinsic fluorescence transients and pyrene-actin transients were fitted to the single $S(t) = S_o+A\cdot\exp(-k_{obs}\cdot t)$, or double exponential function $S(t) = S_o+A_1\cdot\exp(-k_{obs1}\cdot t) + A_2\cdot\exp(-k_{obs2}\cdot t)$, where $S(t)$ is the observed signal at time t, S_o is the final intensity of a signal, A is the signal amplitude, and k_{obs} is the observed rate constant. The dependence of observed rates (v) on the nucleotide concentration was fitted to the hyperbola $v = V_{max}[\mathrm{ATP}]/(K_m+[\mathrm{ATP}])$, according to the steady state approach, allowing determination of V_{max}, maximum kinetic rate, and Michaelis constant K_m.

The rate of ATP-induced myosin.ADP dissociation was determined from the experiments where 0.8 μ*M* myosin was initially incubated with ADP of variable concentrations and then rapidly mixed with 600 μ*M* ATP (syringe concentrations). Myosin intrinsic fluorescence transients were measured, their intensities were normalized to FRET data to determine M** fraction. Reaction rates k_{+6}, obtained for different ADP concentrations were averaged.

Competitive inhibition of ATP-induced actomyosin dissociation by ADP was measured with pyrene-actin, complexed with myosin, and incubated with ADP of variable concentrations. This solution was rapidly mixed with ATP (50 μ*M*, syringe concentration) and the transient of pyrene-actin, dissociated from myosin was measured. Transients were fitted to the single exponential function. The observed reaction rates were normalized to the value of the observed rate in the absence of ADP, $k_{res} = k_{obs}/k_{obs,}$

$_{[ADP]=0}$ and fitted to the equation $k_{res} = 1/(1+[ADP]/ (k'_{+6}K'_7))$, assuming that ATP binding to actomyosin is fast. Here $k'_{+6}K'_7$ is the rate of ADP dissociation from actomyosin.

Differential equations were solved numerically and the solution was fitted to the transients using the Differential Evolution algorithm, realized in Wolfram Mathematica software suite. We used 10,000 search points, scaling factor 2, and cross probability 0.8. Each transient was fitted several times, starting with different initial conditions to be sure that global minimum is found during the fit.

4.3 Results

4.3.1 Myosin Pre- and Post- Recovery Stroke Conformations

Two FRET probes were attached to the designed labeling sites within myosin force generation region (Figure 4-1. The FRET effect between the probes, allowing the interprobe distance measurement and therefore reflecting myosin structure in the force generation region, was virtually the same when myosin was rapidly mixed with Mg-, Mn-, or Ca.ATP. Measured interprobe distance was 4.1 ± 0.94 nm in the M* state and 3.1 ± 0.66 nm in the M** state. Myosin maintains the same pre- and post- recovery stroke conformations (M* and M**) upon interaction with magnesium-, manganese-, or calcium ATP complexes.

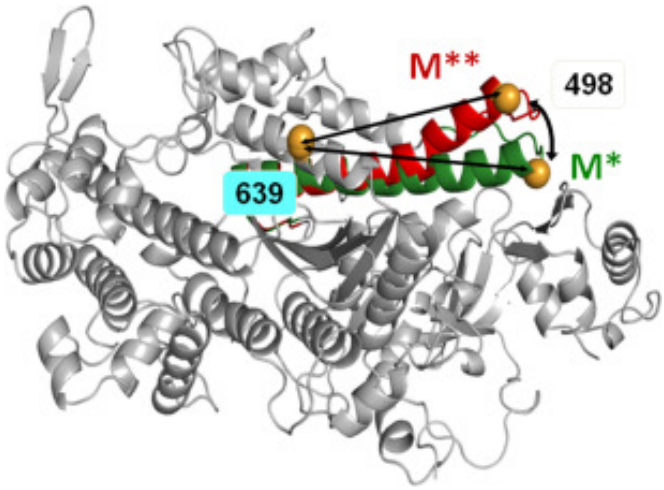

Figure 4-1: *D.discoideum* myosin head structural change during the recovery stroke. Overlay of crystal structures 1FMV (M*) and 1VOM (M**), showing bending of the relay helix. Spheres: engineered labeling sites, showing predicted shortening of distance between A639C and K498C (arrows) during the recovery stroke.

4.3.2 Myosin Structural Change During the Recovery Stroke

Change of myosin intrinsic fluorescence during its interaction with ATP reflects myosin conformational change (34). Myosin head has several tryptophan residues, contributing to intrinsic fluorescence and potentially responsible for the change in the intrinsic fluorescence upon myosin interaction with ATP. The spectral response of these tryptophan residues is similar, so the information on the location of myosin conformational change is missing in the intrinsic fluorescence experiment (35). Single tryptophan studies (36-38) concluded that the main contribution to myosin fluorescence change comes from W501 (*D. discoideum* sequence), although single tryptophan W501 mutant showed unexpected initial decrease of intrinsic fluorescence (36). We have found that kinetics of myosin recovery stroke, measured with FRET, agrees well with the kinetics of the intrinsic fluorescence (Figure 4-2). This result directly confirms that intrinsic fluorescence reflects kinetics of myosin force generation region during the recovery stroke. The distinct advantage of FRET is that it provides quantitative data on the mole fractions of the pre- and post-recovery stroke states M* and M**, in contrast to intrinsic fluorescence, measuring just changes in fluorescence intensity.

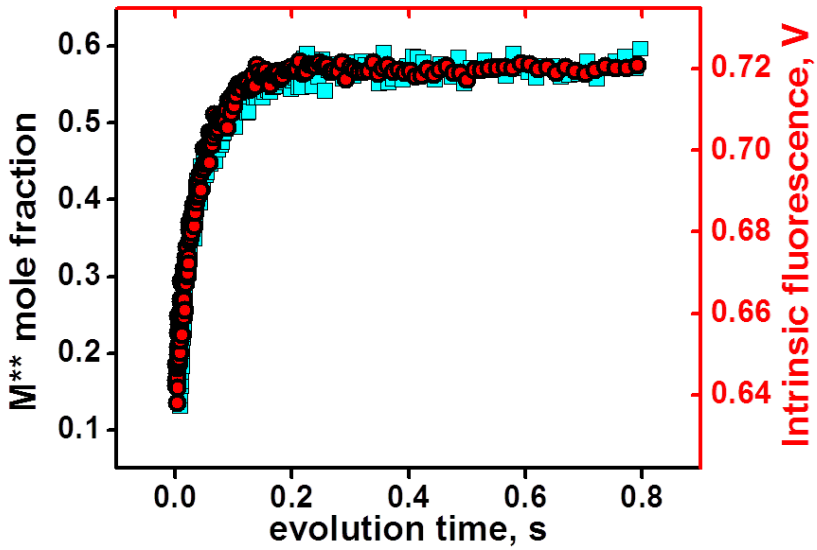

Figure 4-2: Overlay of FRET (squares) and intrinsic fluorescence (circles) transients for myosin Mg.ATPase. 0.8 uM myosin, rapidly mixed with 600uM uM Mg.ATP (syringe concentrations). Intrinsic fluorescence and FRET reflect the same conformational transition in myosin.

4.3.3 Rate Limiting Step of Myosin ATPase

Transients of myosin conformational change upon interaction with metal are shown in Figure 4-3. All metal cations support myosin ATPase activity, showing increase of M** population upon interaction with metal, and then decrease of M** population in the cases of Mn.ATP and Ca.ATP. Figure 4-3 shows that myosin reaches the steady state M** when mixed with Mg.ATP, reflecting that the reaction limiting step is the reverse recovery stroke and the phosphate release. In the presence of manganese, the steady state M* is reached, showing that the reaction rate limiting step is the step after the reverse recovery stroke and the phosphate release. This could be the myosin—ADP isomerization or the ADP release, according to Figure 4-3. Ca.ATP produces fast reached steady state of myosin at the level of ~20% M**, indicating that Ca.ATPase cycle is fast and there is no distinct reaction rate limiting step, myosin spends 20% of the cycle time in the M** structural state. Transients, obtained at

different ATP concentrations, were fitted to Figure 4-3 with the set of differential equations [Eqs. (4.1) (4.2)].

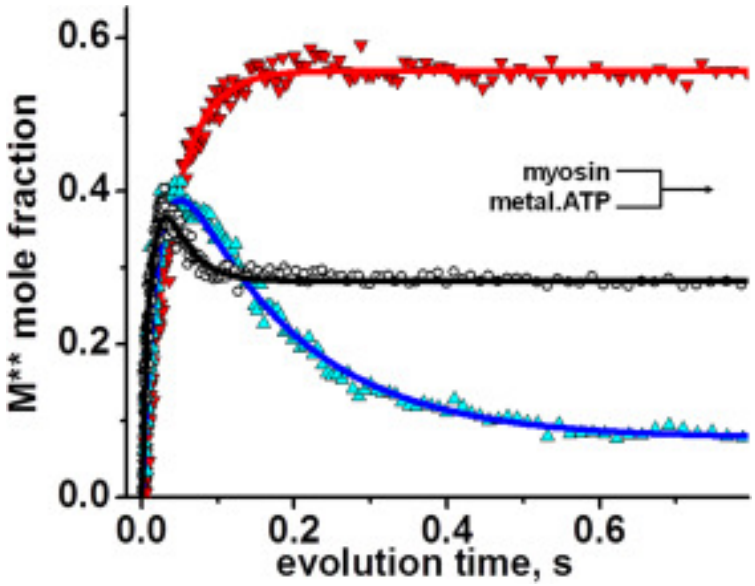

Figure 4-3: Kinetics of the post-recovery stroke M** structural state formation upon rapid mixing of myosin and metal.ATP. Magnesium, upturned triangles, manganese, triangles, calcium, circles, lines, fit. Mg.ATP shifts equilibrium towards M** state, Mn.ATP – towards M* state, indicating that Mn.ADP release is the rate limiting step. Myosin – Ca.ATP interaction produces fast equilibrium of M* and M**, depending on the forward and reverse rate constants. Concentrations after mixing, [ATP]=300 μ*M*, [metal cation] = 3 m*M*, [myosin] = 0.4 μ*M*.

.

$$\frac{d[M]}{dt} = -K_1K_2k_{+3}[M][T] + k_{-3}[M^{**}.D.P] \tag{4.1}$$

$$\frac{d[M^{**}T]}{dt} = K_1K_2k_{+3}[M][T] - k_{-3}[M^{**}.D.P]$$

$$\frac{d[M]}{dt} = -K_1K_2k_{+3}[M][T] + k_{-3}[M^{**}.D.P.] + k_{+6}[M^{*}.D]$$

$$\frac{d[M^{**}T]}{dt} = -K_1K_2k_{+3}[M][T] - k_{-3}[M^{**}.D.P.] - k_{+4}[M^{**}.D.P]$$

$$\frac{d[M^{*}D]}{dt} = k_{+4}[M^{**}.D.P.] - k_{+6}[M^{*}.D] \tag{4.2}$$

$$M + T \underset{k_{-1}}{\overset{k_{+1}}{\rightleftarrows}} M.T \underset{k_{-2}}{\overset{k_{+2}}{\rightleftarrows}} M^{*}.T \underset{k_{-3}}{\overset{k_{+3}}{\rightleftarrows}} M^{**}.D.P \underset{k_{-4}}{\overset{k_{+4}}{\rightleftarrows}} M^{*}.D.P \underset{k_{-5}}{\overset{k_{+5}}{\rightleftarrows}} M^{*}D + P \underset{k_{-6}}{\overset{k_{+6}}{\rightleftarrows}} M.D \underset{k_{-7}}{\overset{k_{+7}}{\rightleftarrows}} M + D$$

Figure 4-4: Myosin ATPase cycle. M - myosin; T - ATP; D - ADP; P - phosphate; M* - myosin in the pre-recovery stroke structural state; M** - myosin in the post-recovery stroke structural state.

In the experiment we observe changes of myosin intrinsic fluorescence, or the change in the FRET effect (FRET technique), therefore the direct information on the first two steps of myosin cycle in Figure 4-4 is missing. Obtained transients (myosin-Mg.ATP, and initial parts of myosin-Mn.ATP and myosin-Ca.ATP transients) can be fitted to the single exponential function, showing that they reflect a single step reaction. We conclude that the first two steps of Figure 4-4 (K_1K_2) are fast and cannot be resolved due to the dead time of our stopped flow units (2.4 ms and 2.6 ms). The fit of myosin-Mg.ATP transient with Eq. (4.1) (assuming step 4 the reaction limiting step), and subsequent fit of observed rate constants k_{obs} to the hyperbola to find maximum rate gives $k_{max} = 20.2 \pm 2.6\ s^{-1}$. This corresponds well to the maximal rate of fluorescence changes of another *D.discoideum* myosin construct (39), and associated with the rate of ATP cleavage k_{+3}. We found that the backward rate is $k_{-3} = 4.8 \pm 3.9\ s^{-1}$. The fit of the same transients to the single exponential function and subsequent fit of the rates to the hyperbola produced $V_{max} = 31.7 \pm 3.9\ s^{-1}$, in good agreement with the fit to Eq. (4-1). Transients of myosin mixed with Mn.ATP and Ca.ATP require more reaction steps to be accounted for. According to the previous studies, the step 4 is practically irreversible (33, 40), the step 5 is fast (33) and irreversible, therefore the rate constant k_{+4} determines the rate of the reverse recovery stroke and the phosphate release. The rate constant k_{-6} and k_{+7} are fast (33), therefore the state M.D is not populated. Assuming that the rate of ADP binding to myosin is the same as the rate of ATP binding (33), and considering significant difference in ATP and ADP concentrations in the reaction, we do not expect M.D state be populated due to myosin-ADP association. Therefore, the transients of myosin mixed with Mn.ATP or Ca.ATP were fitted to Eq. (4.2), and the results are shown in Table 4-1.

Table 4-1: The rates of kinetic steps of myosin ATPase cycle (Figure 4-4) with metal.nucleotide as a ligand

Cation	Ionic radius, Angstroms	Coordination number	k_{+3}, s^{-1} recovery stroke, forward rate	k_{-3}, s^{-1} recovery stroke, backward rate	k_{+4}, s^{-1} reverse recovery and Pi release	k_{+6}, s^{-1} myosin.ADP isomerization and ADP release
Mg^{2+}	0.72	6	20.2±2.6	4.8±3.9	0.25±0.03*	0.65±0.08**
Mn^{2+}	0.83	6	58.3±11.6	4.7±5.0	8.6±0.7	0.85±0.17
Ca^{2+}	1.0	7	67.6±15.8	22.0±7.3	22.4±2.6	16.9±4.1

*The rate of basal ATPase, in assumption that the reverse recovery stroke and the phosphate release is the rate limiting step.
**Data from ATP chase experiment.

The rate of Mg.ADP release from myosin was measured with the ATP chase experiment, when myosin pre-mixed with Mg.ADP was rapidly mixed with Mg.ATP, and the recovery stroke was observed. The rate constant k_{+6}, reflecting Mg.ADP dissociation from myosin, is shown in Table 4-1. The rates of Mn.ADP and Ca.ADP dissociation from myosin were determined from the fit of myosin-ATP transients. Omitting the step of ADP dissociation in the fit significantly decreases the fit quality.

4.3.4 ATP Binding and ADP Release from Actomyosin

The rates of metal.nucleotide binding to actomyosin were determined with the pyrene-labeled actomyosin, rapidly mixed with metal.ATP. Pyrene fluorescence was monitored to measure ATP-induced actomyosin dissociation (Figure 4-5, left). Transients of pyrene fluorescence were fitted to the double exponential function. Fast exponential reflects ATP binding, and slow exponential reflects conformational change at the nucleotide binding site of myosin and subsequent actomyosin dissociation (41). Obtained rates of the fast component at small ATP concentrations were fitted to the straight line (Figure 4-5, right). The second order reaction rate, determined from the slope of the line, shows virtually the same rate of Mg- and Mn.ATP binding to

actomyosin (1.6 μM^{-1} s^{-1}) and approximately four times lower rate for Ca.ATP binding (0.35 μM^{-1} s^{-1}, Table 4-2), indicating that ATP binding to actomyosin depends on the cation coordination number.

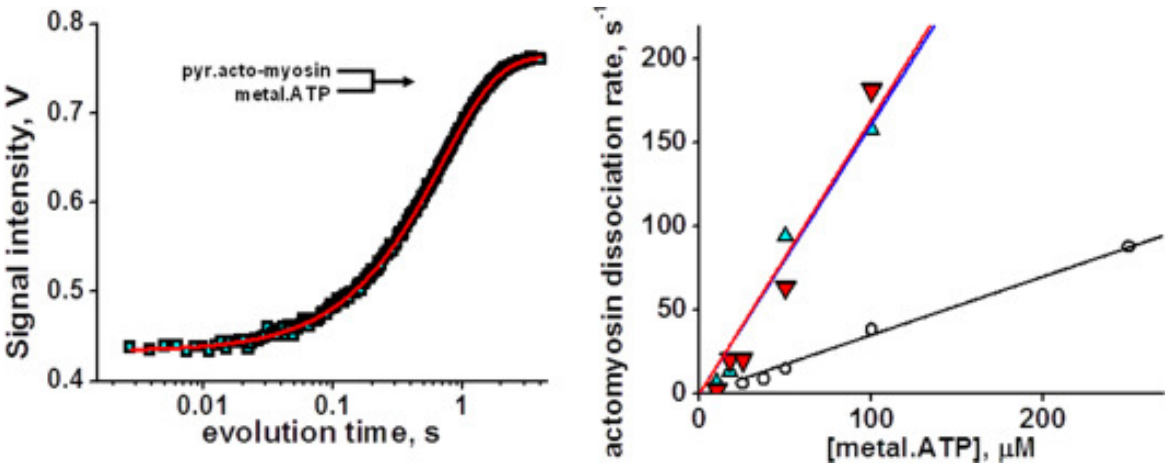

Figure 4-5: ATP-induced actomyosin dissociation. Left, pyrene fluorescence transient after rapid mixing of 50 μ*M* ATP and 0.15 μ*M* pyrene.acto-myosin, fitted with two exponents. Right, dependence of observed rate constants of actomyosin dissociation (fast exponential component) on ATP concentration. Magnesium, upturned triangles, manganese, triangles, calcium, circles, lines, linear fit. The second order reaction rate constant of actomyosin dissociation is determined from the slope of the line, 1.6 $\mu M^{-1}s^{-1}$ (magnesium and manganese), and 0.35 μM^{-1} s^{-1} (calcium). Slow exponential component represents [ATP] independent myosin isomerization, probably nucleotide pocket opening (22).

ATP binding to pyrene-labeled actomyosin premixed with ADP reflects the affinity of ADP to actomyosin. Figure 4-6 shows normalized rates of ATP-induced actomyosin dissociation in the presence of different ADP concentrations and the fit to determine the rate of ADP dissociation from actomyosin, $k'_{+6}K'_7$(42). The asterisk indicates actin presence, and the scheme of the reaction is the same as Figure 4-4, but with actin, bound to myosin. Figure 4-6 shows that affinity of Ca.ADP to actomyosin is 2–3 times weaker than affinities of Mg.ADP and Mn.ADP (Table 4-2), indicating the dependence of ADP dissociation from actomyosin on the cation coordination number.

Table 4-2: The rates of kinetic steps of actomyosin ATPase cycle with metal.nucleotide as a ligand

Cation	Ionic radius, Angstroms	Coordination number	Actin binding to myosin.ADP, μM^{-1} s^{-1}	ATP induced actomyosin.ADP dissociation, μM	ATP induced actomyosin dissociation, μM^{-1} s^{-1}
Mg^{2+}	0.72	6	1.69 ± 0.13	16.7 ± 1.9	1.64 ± 0.16
Mn^{2+}	0.83	6	1.29 ± 0.39	11.2 ± 1.6	1.71 ± 0.29
Ca^{2+}	1.0	7	1.61 ± 0.26	34.1 ± 3.7	0.35 ± 0.01

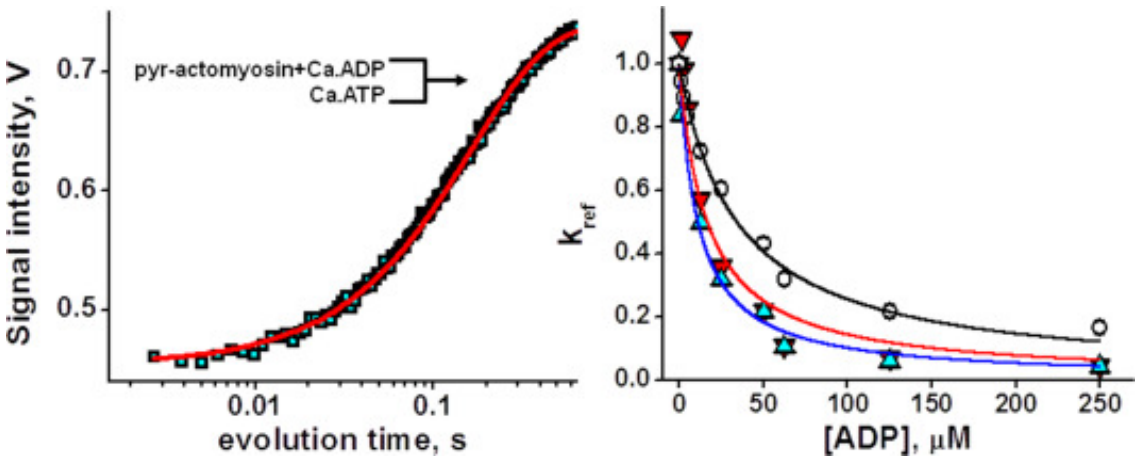

Figure 4-6: ATP induced actomyosin dissociation in the presence of ADP. Left, pyrene fluorescence transient after rapid mixing of 50 µ*M* Ca.ATP and 0.15 µ*M* pyrene-actomyosin, premixed, and incubated with 50 µ*M* Ca.ADP. Fit with one exponent. Right, normalized rates of ATP induced actomyosin dissociation in the presence of ADP. Magnesium, upturned triangles, manganese, triangles, calcium, circles, lines, fit. Ca.ADP has weaker affinity to actomyosin, compared with Mg.ADP and Mn.ADP.

4.3.5 Actin Binding to Myosin

ADP is not affected by metal cation. The rates of actin binding are similar and the dependence of the rates on ADP concentration are the same for magnesium-, manganese- and calcium-ADP complexes (Table 4-2).

4.3.6 Actin Activation of Myosin Metal ATPase

The rates of actin activated and basal myosin ATPase in the presence of magnesium, manganese, or calcium cations are shown in Table 4-3 and Figure 4-7. We were not able to obtain a good fit of actin activated Ca.ATPase rates with the standard Briggs-Haldane equation (43). Addition of a constant term to the Briggs-Haldane equation significantly increased the fit quality (Figures 4-8, 4-9). This constant term is

interpreted as an admixture of the basal Ca.ATPase activity to the actin activated myosin ATPase activity. Both actin activated and basal ATPase rates depend linearly on metal cation radius, with virtually the same slopes, showing that actin activation does not depend on the size of metal cation, complexed with ATP. Apparently, actin directly affects myosin structural transition M** → M*, forcing myosin power stroke. The independence of actin activation on metal cation indicates that the mechanism of actin activation is different from the effect of metal cation (Mn and Ca), destabilizing myosin active site and thus inducing the reverse recovery stroke in myosin.

Table 4-3: The rates of myosin basal and actin activated ATPase activity with metal.ATP as a ligand

Cation	Ionic radius, Angstroms	Coordination number	Experimental data		Actin activation, s^{-1}	Km, Michaelis constant
			Basal ATPase, s^{-1}	Actin activated ATPase, s^{-1}		
Mg^{2+}	0.72	6	0.25 ± 0.04	3.73 ± 0.36	3.48 ± 0.36	39.8 ± 7.3
Mn^{2+}	0.83	6	1.19 ± 0.20	5.66 ± 0.20	4.46 ± 0.04	49.5 ± 13.1
Ca^{2+}	1.0	7	3.86 ± 0.71	7.92 ± 0.75	4.06 ± 0.23	50.0 ± 33.0

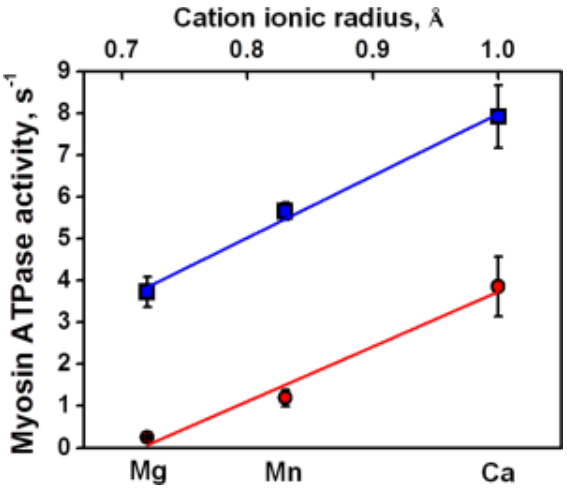

Figure 4-7: The rates of myosin metal.ATPases, basal, circles, and actin activated, squares. Fitting lines have the same slope, showing that the actin activation is the constant value and does not depend on metal cation.

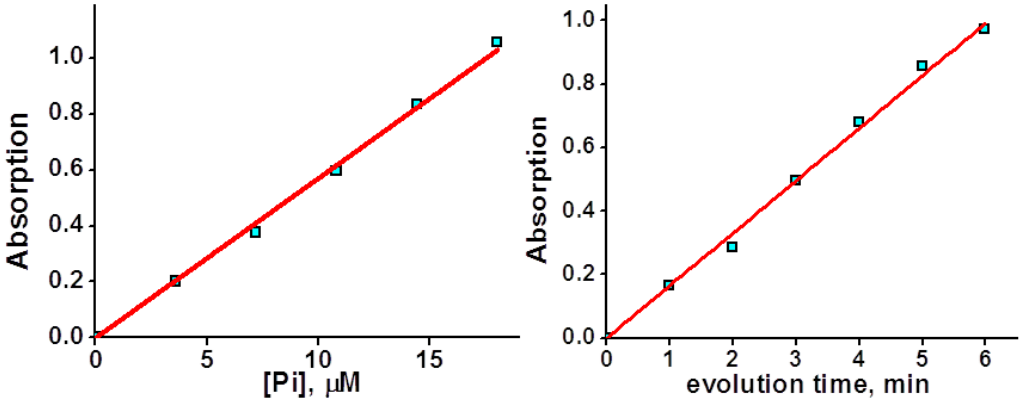

Figure 4-8: Basal myosin ATPase activity measurement. Left, phosphate absorption. Phosphate aliquots of known concentration added to the reagent consisted of 1% of ammonium molybdate, 0.0325% of malakhite green, and 2% of Sterox in 1N HCl. 34% sodium citrate in 1N HCl added to the mixture in 30 seconds to stabilize color formation. Absorption at 620 nm recorded in 10 minutes after citrate addition. Right, time resolved phosphate production by myosin ATPase upon mixing with ATP. Myosin was mixed with ATP (T=25°C) and 50uL aliquots were taken each minute and added to the reagent. Sodium citrate was added in 30 seconds and absorption of the mixture was read after 10 minutes.

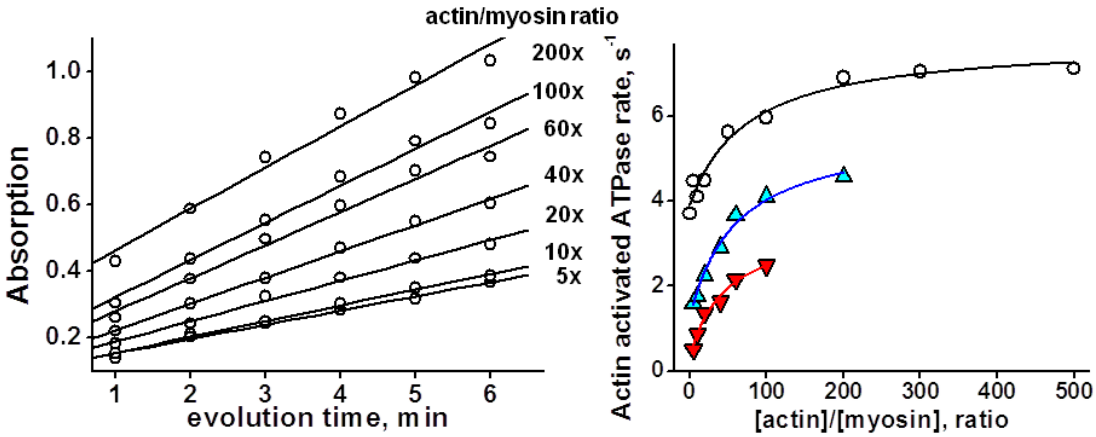

Figure 4-9: Measurement of the rate of actin activated myosin ATPase. Left, time resolved phosphate production by myosin, premixed with actin at different ratios, and then mixed with ATP. Right, observed rates of actin activated myosin ATPase, fitted to the modified Briggs-Haldane equation $v = V_{basal} + V_{max}[actin]/(K_m + [actin])$, where v is the rate of the ATPase in the presence of actin, V_{basal} is the rate of myosin ATPase without actin, V_{max} is the rate of myosin ATPase at infinite actin concentration, and K_m is the Michaelis constant. Magnesium, upturned triangles, manganese, triangles, and calcium, circles.

4.4 Discussion

FRET has two distinct advantages in transient kinetic measurements. First, the mole fraction of protein conformations is determined in the FRET experiment. FRET effect is reciprocally proportional to the distance between donor and acceptor probes attached to the protein, and protein conformations are discriminated by the interprobe distance. FRET effect is proportional to the number of FRET donor-acceptor pairs

(protein molecules), which allows determination of the mole fraction of each protein conformation. Second, FRET allows localization of the transient conformational change within the molecule, due to known position of FRET donor-acceptor pair. These make FRET a structural kinetics technique, in which determination of interprobe distance provides quantitative measure of molecular structure in transient experiment with millisecond time resolution.

Magnesium, manganese, and calcium, complexed with ATP, support myosin ATPase activity, showing that myosin is a nonspecific enzyme, binding, and hydrolyzing different metal.ATP complexes. The timing of myosin and actomyosin kinetics changes with different metal.ATP complexes, confirming that myosin and cross-bridge kinetics can be modulated. This opens up a possibility to modify myosin function directly, introducing changes in myosin's natural ligand, the metal nucleotide complex.

We found that the rate of myosin conformational change depends on the cation size. We suggest that the bigger cation at the active site destabilizes the salt bridge R238:E459 (*D.discoideum* sequence) between Switch I and Switch II loops (44), promoting faster phosphate release and thus increasing the rate of myosin conformational changes.

Kinetic rates of myosin ATPase cycle and the rate of basal ATPase activity. The rate of basal Mg.ATPase activity is slower than measured rates of Mg.ATP binding and the recovery stroke, and slower than the rate of Mg.ADP release, which allows assigning the rate of basal Mg.ATPase as the rate of the reverse recovery stroke and the phosphate release. The rate of myosin.Mn.ADP isomerization and Mn.ADP release corresponds well with the rate of basal Mn.ATPase, allowing assignment of Mn.ADP release as a rate limiting step. For calcium, all measured rates of myosin ATPase cycle

are faster than the measured rate of basal ATPase. The rate of myosin basal Ca.ATPase is determined in the assumption that all myosin molecules perform ATPase cycle. To correlate our transient data and the steady state myosin Ca.ATPase results, we propose that not all myosin molecules participate in Ca.ATPase cycle. Then, the slowest kinetic step should limit myosin Ca.ATPase activity (myosin.ADP isomerization and ADP release, $K_6K_7 = 17\ s^{-1}$). Normalization of the basal Ca.ATPase rate to the slowest kinetic step rate gives 20% myosin molecules, participating in the Ca.ATPase activity. This number corresponds well to the kinetic trace of Figure 4-3, showing reached equilibrium of Ca.ATPase at the level of ~20% M**, indicating that in the any moment no more than 20% of myosin molecules are in M** structural state and the rest of them are in M* state.

Actin activation of myosin ATPase does not depend on metal cation, complexed with ATP. This indicates that the mechanism of actin activation has different nature than the mechanism of myosin ATPase rate modulation by metal cation. We propose that the bigger metal cation destabilizes myosin active site, which follows by faster release of products of hydrolysis and then initiating faster myosin conformational change. We propose that actin binding destabilizes myosin's pre-power stroke conformation and initiates the power stroke, followed by faster release of products of hydrolysis.

Our data suggest independence of actin activation and the modulation of myosin ATPase activity by metal cation. To account for this independence we modified the steady state Briggs-Haldane equation (43), similarly to the standard analysis of solute uptake for two independently operating uptake systems, where the solute concentration is the independent variable, and the measured uptake rate is the dependent variable. This approach allowed us fitting all ATPase activity experimental data within one

model, assuming simultaneous basal and actomyosin ATPase activities. The independence of mechanisms of myosin ATPase activation allows estimation of the probability of actomyosin futile cycle as the ratio of V_{basal} and V_{total} ($V_{total} = V_{basal} + V_{max}$, where V_{max} is the maximum rate of actin activated myosin ATPase). Then, for Mg.ATP it is $V_{basal}/V_{total} = 5.9\%$, Mn.ATP – 22.9%, and Ca.ATP – 49.1%. Manganese and calcium ATP complexes increase the rate of actomyosin ATPase cycle, but make it less efficient in terms of the force production.

4.5 Conclusions

We have studied myosin and actomyosin kinetics, using Mg, Mn, and Ca complexed with ATP as a ligand. All three cations have different ionic radii for octahedral coordination, 0.072 nm (magnesium), 0.083 nm (manganese), and 0.1 nm (calcium). Both magnesium and manganese cations maintain octahedral ligand coordination geometry. Calcium belongs to the same group in the periodic table as magnesium, but its larger size makes it maintaining irregular coordination geometry with the coordination number seven. Therefore, in this work we studied the effect of the ionic radius and the coordination number of the metal cation in the metal.ATP complex on myosin and actomyosin kinetics. We used previously characterized double-Cys *D. discoideum* myosin construct (A639C:K498C) (32), labeled with IAEDANS:Dabcyl FRET pair (Figure 4-1). We thoroughly studied myosin and actomyosin steady state ATPase activities. We employed the collection of transient spectroscopic techniques, based on the transient time resolved FRET (TR^2FRET), myosin intrinsic fluorescence, and the fluorescence of pyrene labeled actin. We measured rates of myosin conformational changes upon interaction with metal.ATP, and actomyosin association and dissociation in the presence of the nucleotide (33). In the result, we conclude that the rate of myosin conformational changes, the recovery

and the reverse recovery strokes, are proportional to the cation ionic radius. The cation coordination number affects the rate of the nucleotide binding to and release from myosin and actomyosin. We found that actin activation of myosin ATPase is constant and does not depend on metal cation, suggesting that the mechanism of actin activation is different from the mechanism of myosin ATPase modulation by different metal cations. FRET was a critical resource for the quantitative conclusions in this study, due to the resolution of FRET technique to the mole fractions of myosin conformational states M* and M** during interaction with the nucleotide.

CHAPTER 5: MACROMOLECULAR CROWDING MODULATES ACTOMYOSIN KINETICS

5.1 Introduction

Actomyosin kinetics is usually studied in dilute solutions at low protein concentrations or in a single-molecule setup, which is dramatically different from the highly structured protein organization of the sarcomere or the dense cytoplasm environment with macromolecular content reaching 20–30% w/v. Such a high macromolecular concentration results in significant volume exclusion (45, 46). Due to the excluded volume, the space available to solutes decreases, which 1) forces the macromolecular solutes to accept a more compact form to minimize their excluded volume (47), and 2) effectively increases the solutes' concentration, thus increasing their chemical potential. The chemical potential of small solutes is less affected by crowding than that of the large ones, since the excluded volume depends on the sum of radii of the solute and the macromolecular crowder. In the actomyosin cycle, myosin interacts with two ligands: a relatively small nucleotide and a much larger actin. Therefore, the actomyosin cycle potentially can be modulated by crowding, and one can expect different effects of crowding on the activity of myosin ligands.

Our goal in this work was to examine whether macromolecular crowding indeed affects the kinetics of the actomyosin cycle. We used buffered solutions of *Dictyostelium discoideum* myosin II, rabbit skeletal actin, ATP, ADP, and 25% w/v Ficoll PM 70 (Ficoll70) as a crowding agent to mimic the crowding effect of the intracellular environment (48-51). Ficoll70 is a nonionic cosolvent with a molecular radius of 5.1 nm and a molecular mass of 70 kDa, and thus is comparable in size and

mass to myosin head (89 kDa, prolate spheroid with axes 10.05 nm and 16.25 nm (52)). Ficoll70 stabilizes proteins in solution, but does not form a stable complex with them (51). For the crowded solution, we anticipated 1) a slight increase in the rate of nucleotide binding to myosin and actomyosin, 2) a significant increase in the strong actomyosin complex formation rate, 3) a slight inhibition of ADP dissociation from actomyosin due to the increased effective concentration of ADP in solution, 4) no effect on the rates of actomyosin dissociation and the recovery stroke, and 5) no change in the overall rate of the cycle. A faster entry into strong actomyosin binding and a slower exit from it should affect the myosin duty ratio, which is determined as the time myosin spends being strongly bound to actin relative to the overall time of the cycle.

5.2 Experimental

5.2.1 Sample Preparation

An A639C:K498C mutant of *Dicty.* myosin S1 was expressed and purified as described previously. The myosin concentration was determined spectrophotometrically assuming an extinction coefficient of $A_{280nm} = 0.69\ (mg/mL)^{-1}cm^{-1}$. For FRET measurements, the protein was labeled in two steps: 1) with the donor (IAEDANS) and 2) with the acceptor (DABCYL). Unreacted probes were removed by spin concentration (Amicon Ultra; EMD Millipore, Billerica, MA). Labeled myosin was centrifuged at 100,000 g for 40 min to remove possible aggregates. The concentration of labeled myosin was determined by a Bradford assay (Bio-Rad Laboratories, Hercules, CA). Actin was prepared from rabbit back and leg muscles as described previously. F-actin was labeled with pyrene iodoacetamide or TEMPO maleimide (6:1 label/actin molar ratio), cleaned from the excess label, repolymerized, stabilized with phalloidin at a molar ratio of 1:1, and dialyzed for 2 days at T = 4°C

against the experimental buffer. The concentration of unlabeled G-actin was determined spectrophotometrically assuming an extinction coefficient of $A_{290\,nm} = 0.63$ $(mg/mL)^{-1}cm^{-1}$. The concentration of labeled G-actin and the labeling efficiency were determined spectroscopically using the following expressions: [G-actin] = (A290nm – ($A_{344nm} \times 0.127$))/26,600 M^{-1} and [pyrene] = A_{344nm}/22,000 M^{-1}.

The experimental buffer contained 20 mM MOPS pH 7.5, 50 mM KCl, with 3mM MgCl2. A 40% w/v Ficoll PM 70 (Amersham Biosciences AB, Uppsala, Sweden) stock solution was prepared first. The Ficoll70 stock solution was diluted to 25% w/v by addition of myosin or actin-buffered solution, or experimental buffer. We obtained 5-((((2-iodoacetyl)amino)ethyl)amino)naphthalene-1-sulfonic acid (IAEDANS) and N-(1-pyrene)iodoacetamide (pyrene) from Life Technologies (Grand Island, NY), DABCYL (4-((4-(dimethylamino)phenyl) azo)benzoic acid) C2 maleimide from AnaSpec (Fremont, CA), and phalloidin, ATP, and ADP from Sigma-Aldrich (Milwaukee, WI). All other chemicals were obtained from ThermoFisher Scientific (Waltham, MA) and VWR (Radnor, PA)

5.2.2 ATPase Assays

Steady-state basal and actin-activated myosin ATPase activities were measured spectrophotometrically at $T = 20°C$ in the experimental buffer with and without 25% w/v Ficoll70 by the liberation of inorganic phosphate as described previously.

The transient intrinsic fluorescence of myosin and the fluorescence of pyrene actin were measured with a Bio-Logic SFM-300 stopped-flow transient fluorimeter (Bio-Logic Science Instruments SAS, Claix, France) equipped with an FC-15 cuvette. The mixing unit dead time was 2.6 ms. All experiments were done at $T = 20°C$. Usually, three syringes and two mixers were used in an experiment. Continuous flow and the smallest intermixer delay line (40 μL) were used except in the weak-to-strong-binding

transition experiment, in which intermittent flow and a 60 μL delay line were used. The delay time of the weak-to-strong binding transition experiments was adjusted to make sure that the maximum concentration of myosin in the M** state would be produced in the first mixing. Myosin intrinsic fluorescence was excited by a mercury-xenon lamp at 296 nm and detected using a 320 nm cutoff filter. The pyrene fluorescence was excited at 365 nm and detected using a 420 nm cutoff filter. Multiple transients were usually acquired and averaged to improve the signal/noise ratio. A total of 8000 points were acquired in each experiment.

5.2.3 Analysis of Fluorescence Transients

The transients obtained in each experiment were fitted globally by the single exponential function $S(t) = S_o + A \cdot \exp(-k_{obs} \cdot t)$,, where $S(t)$ is the observed signal at time t, A is the signal amplitude, and k_{obs} is the observed rate constant. The dependence of the observed rates on the nucleotide or protein concentration was fitted by a hyperbola, $v = V_{max}[ATP]/(K_d + [ATP])$,, allowing the determination of the maximum rate, V_{max} (the horizontal asymptote of the hyperbola). To determine the bimolecular rate, the dependence of the observed rates on the nucleotide or protein concentration was fitted by a straight line at small concentrations of the nucleotide or protein. Competitive inhibition of ATP-induced actomyosin dissociation by ADP was measured with pyrene-labeled actin complexed with myosin and incubated with ADP at various concentrations. This solution was rapidly mixed with ATP and the transient fluorescence of pyrene-actin dissociated from myosin was measured. Transients were fitted by singleexponential functions. The observed reaction rates were fitted by the equation $k_{obs}/k_0 = 1/(1+[ADP]/K`_5)$, assuming a small [ATP], using the $k_0$ determined in the experiment without ADP, and varying $K`_5$, which is the constant of ADP dissociation from actomyosin upon chasing with ATP. All data fits were performed

with Origin 8 (OriginLab, Northampton, MA). Ficoll70 was fluorescent in the spectral range of our experiments, and its fluorescence exhibited photobleaching. The transient fluorescence of the Ficoll70-buffered solution was measured before each experiment. The observed transient was fitted with a polynomial function, which was then subtracted from the transients obtained in other experiments.

FRET was measured with an in-house-built transient fluorimeter equipped with an SX-18 stopped-flow unit (Applied Photophysics, Leatherhead, UK), passively Q-switched microchip YAG laser (SNV-20F-100, 355 nm, 20 kHz; Teem Photonics, Meylan, France), photomultiplier (H6779-20; Hamamatsu, Middlesex, NJ), and fast digitizer (Acqiris DC252; Agilent, Santa Clara, CA). A 420 nm cutoff filter and a polarizer set at the magic angle were used in the detection arm. The dead time of the mixing unit was 2.4 ms. All experiments were done at T = 20°C. FRET pair-labeled myosin was rapidly mixed with ATP solution, and the donor fluorescence waveform was acquired after each laser pulse with picosecond resolution. Multiple traces were acquired and averaged to increase the signal/noise ratio. Before each experiment, the fluorescence transients of the Ficoll70-buffered solution were measured. All transients acquired in the experiment were corrected for Ficoll70 fluorescence to account for Ficoll70 photobleaching.

5.3 Results

5.3.1 Rate of Actin-Activated Myosin ATPase

The maximum velocity of steady-state, actin-activated myosin ATPase increased by 30% in the Ficoll70 solution (Figure 5-1 A; Table 5-1). The steady-state myosin ATPase activity was determined at the saturated substrate level, and the velocity of the reaction was described by zero-order kinetics independently of the substrate concentration and the volume excluded by Ficoll70. Addition of Ficoll70 did not affect

the rate of basal myosin ATPase activity (Figure 5-1 B). Therefore, the actin activation, determined as the ratio of the rates of the actin-activated to the basal myosin ATPase activity, increased from 18-fold without Ficoll70 to 23-fold in the crowded environment.

Table 5-1 Actomyosin kinetic rate constants with and without Ficoll70

Kinetic step	**No Ficoll70**	**With Ficoll70**
Actomyosin dissociation, $K`_1k`_{+2}$, $\mu M^{-1}s^{-1}$	1.247 ± 0.177	0.094±0.089
Actomyosin dissociation, V_{max}, s^{-1}	431.6 ± 120.1	9.4 ±1.4
ATP binding to myosin, K_1k_{+2}, $\mu M^{-1}s^{-1}$	0.26 ±0.05	0.11±0.01
Recovery stroke and hydrolysis, V_{max}, s^{-1}	34.9±4.4	10.0±0.9
Weak to strong binding transition, $K_8k`_{+4}$, $\mu M^{-1}s^{-1}$	0.13 ± 0.01	0.05 ± 0.01
ADP release from acto-myosin, $K`_5$, μM	1.07 ±0.07	1.58 ±0.58
Basal myosin ATPase, (mole Pi)/(mole myosin)s^{-1}	0.140±0.007	0.133±0.002
Actin-activated myosin ATPase, V_{max}, s^{-1}	2.5±0.1	3.1±0.1
Actin activation, actin activated/basal ATPase	17.9±1.1	23.3±0.8

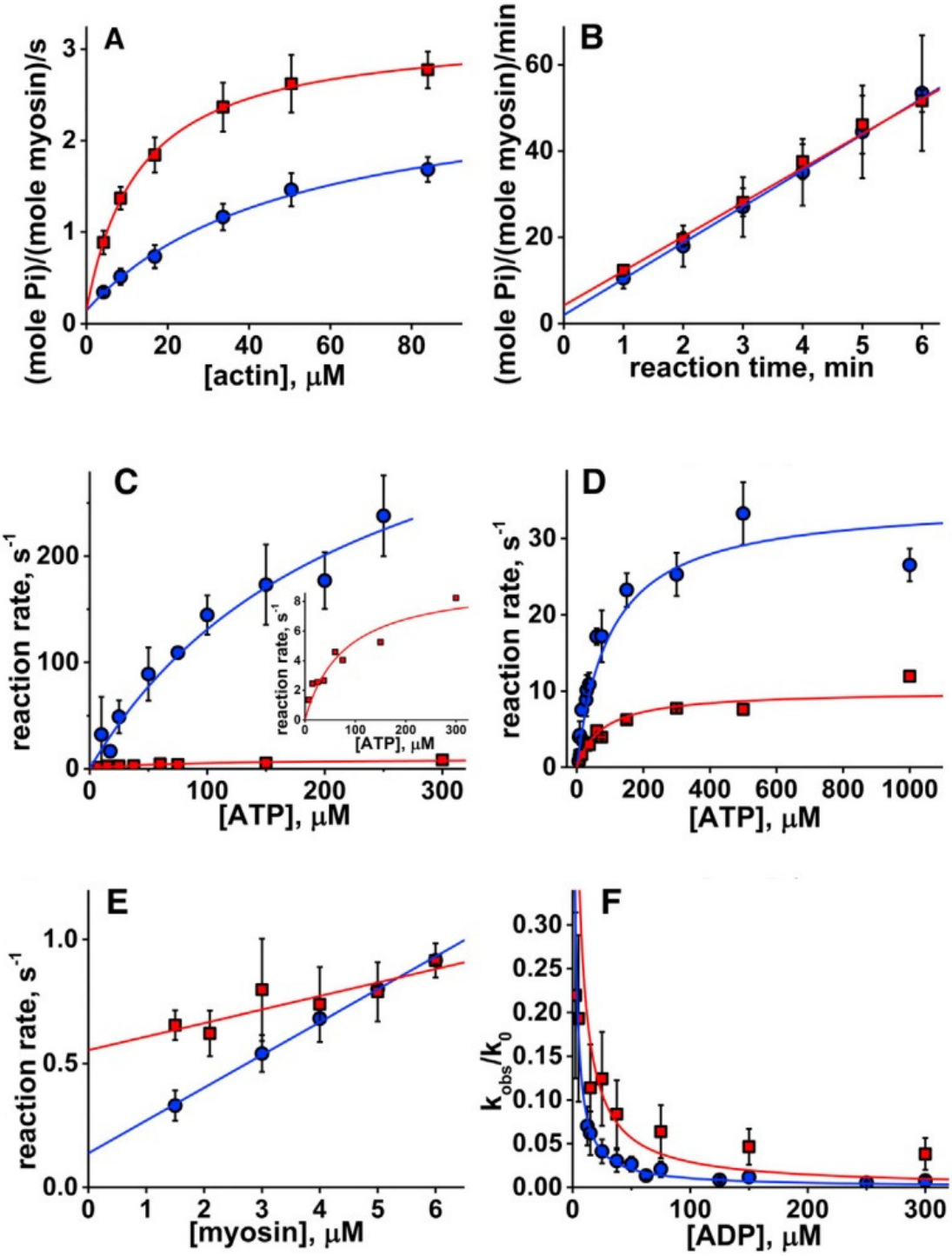

Figure 5-1. (A) Steady state, actin-activated myosin ATPase activity ([myosin] = 0.8μM, [ATP] = 5mM; *circles*, no Ficoll70; *squares*, with Ficoll70 in solution). Fit with hyperbola, V_{max} = 2.5 ± 0.1 s^{-1}, no Ficoll70; and 3.1 ± 0.1 s^{-1} with Ficoll70. The data points are average of *N*=6 independent protein preparations. Uncertainties are standard deviation here and throughout the text. (B) Basal myosin ATPase activity, [myosin]=3.3uM. Linear fit, *N*=6, v = 0.140 ± 0.007 s^{-1}. no Ficoll70; and 0.133 ± 0.002 s^{-1} with Ficoll70. (C) ATP-induced actomyosin dissociation. No Ficoll70, *N* = 6, with Ficoll70 in solution, *N* = 2. Fit with hyperbola, V_{max} = 431.6 ± 120.1 s^{-1}, no Ficoll70; and 9.4 ± 1.4 s^{-1} with Ficoll70. Inset: data obtained with Ficoll70 in solution. (D) Kinetics of ATP binding and the recovery stroke upon rapid mixing of myosin and ATP, observed rate constants are fitted to hyperbola, V_{max} = 34.9 ± 4.4 s^{-1}, *N*=4, no Ficoll70; and 10.0 ± 0.9 s^{-1} *N* = 2 with Ficoll70 in solution. (E) Kinetics of the weak to strong transition of acto-myosin binding,

N=4. The observed reaction rates are fitted to a straight line, and the second order reaction rate constant is determined from the slope of the line. $K_8k`_{+4}$ = 0.13 ± 0.01 $\mu M^{-1}s^{-1}$ no Ficoll70; and 0.05 ± 0.01 $\mu M^{-1}s^{-1}$ with Ficoll70 in solution. (F) ATP induced ADP dissociation from actomyosin ([actomyosin] = 0.5μM, [ATP] = 25 μM; *circles*, no Ficoll70, *N* = 3; s*quares*, with Ficoll70, *N*=2). Lines: fit by the model of competitive inhibition with variable parameter $K`_5$, $K`_5$ = 1.07 ± 0.07 μM, no Ficoll70; and 1.58 ± 0.58 μM with Ficoll70.

5.3.2 ATP-Induced Actomyosin Dissociation

The rate of ATP-induced actomyosin dissociation was measured with 0.5 mM pyrene actomyosin (the concentration in the final mixture, here and throughout the text) rapidly mixed with various concentrations of ATP (steps 1 and 1, Figure 5-2). Actomyosin dissociation was monitored via an increase of pyrene fluorescence and fitted by a single exponential function (Figure 5-3).

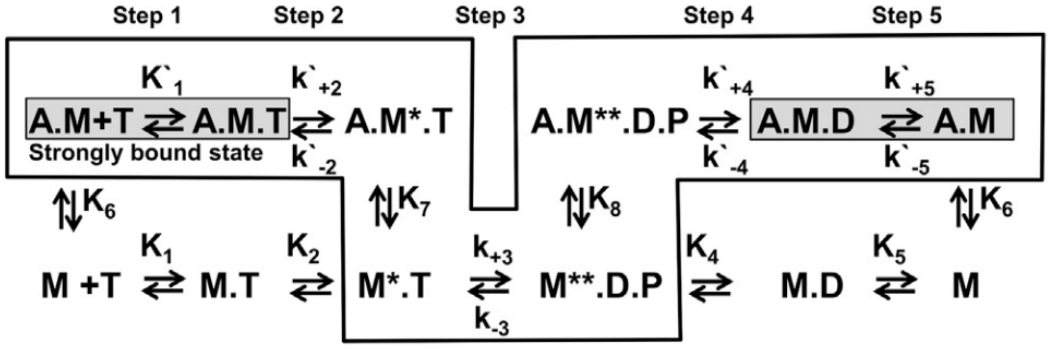

Figure 5-2: Actomyosin ATPase cycle reaction scheme. A, actin; M, myosin (M* and M** indicate myosin states with increased intrinsic fluorescence); T, ATP; D, ADP; P, phosphate. The asterisk indicates reaction rate constants that describe actomyosin kinetics. Highlighted: the strongly bound actomyosin state. Boxed: the generally accepted pathway of actomyosin interaction.

The obtained dependence of the reaction rates on the ATP concentration was fitted with a hyperbola (the maximum rate of actomyosin dissociation V_{max} is a horizontal asymptote determined in the fit; Figure 5-1 C). V_{max} decreased 45-fold upon addition of Ficoll70 to the solution (Table 5-1). The second-order reaction rate constant was determined from the slope of the straight line, fitted to the data points at low [ATP]. Without Ficoll70 in solution, the second-order rate constant was in excellent agreement with the corresponding rates obtained for other D. discoideum constructs (53, 54). With Ficoll70 in solution, the second-order rate constant decreased 12-fold (Table 5-1).

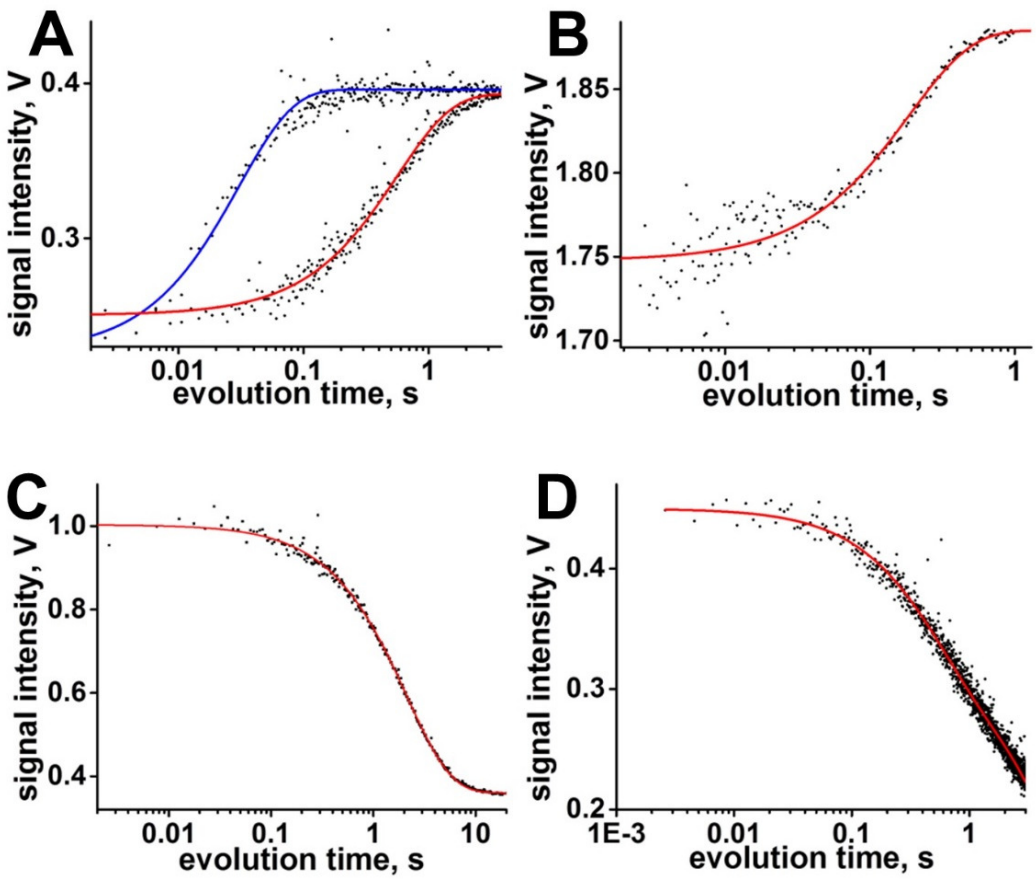

Figure 5-3: (A) Transients of ATP-induced pyrene acto-myosin dissociation, without (blue) and with (red) 37 uM ADP in solution. [actomyosin]=0.5 μM, [ATP]=25 μM. The lines represent single-exponential fits. The obtained rates are 32.8±1.0 s^{-1} and 1.77±0.04 s^{-1}, respectively. (B) Intrinsic fluorescence transient after rapid mixing of 0.5 uM myosin and 18 μM ATP, step 3, Figure 5-2. Line, a single-exponential fit. (C) Transient of the weak to strong binding of actomyosin (step 4, Figure 5-2) in a double mixing experiment. 3 μM myosin, prepared in the post-recovery M** state by rapid mixing with 100 μM ATP and following incubation of the reaction mixture for 2s, rapidly mixed with 0.3 μM actin and 1 mM ADP to quench the reaction. Decrease of pyrene fluorescence shows kinetics of the strongly bound state formation. Line, a single-exponential fit. (D) Transient of actomyosin rigor binding. 0.15 uM pyrene actin rapidly mixed with 0.9 μM myosin. Decrease of pyrene fluorescence shows kinetics of the strongly bound state formation. Line, a single-exponential fit.

5.3.3 ATP Hydrolysis Rate

The rate of the recovery stroke and hydrolysis was measured by rapidly mixing 0.5 μM myosin and ATP (12.5–300 μM) and monitoring the increase in myosin intrinsic fluorescence (55) (step 3, Figure 5-2). The observed intrinsic fluorescence transients were fitted with single-exponential functions (Figure 5-3 B), and the dependence of the obtained reaction rates on [ATP] was fitted by the hyperbolic equation (Figure 5-1 D and 5-2). The maximum rate of myosin fluorescence intensity change (V_{max}) measures the rate of ATP hydrolysis, $k_{+3}+k_{-3}$ (39, 56), assuming that step 3 consists of two distinct

but coupled substeps: the fast and reversible recovery stroke (step 3a) and the hydrolysis step (step 3b), which drives the reaction forward (57). Therefore, the kinetics of the hydrolysis step decreased 3.5-fold in the presence of Ficoll70 (Table 5-1). Both with and without Ficoll70, V_{max} was fast enough to be nonlimiting for the overall rate of the actomyosin cycle. The association rate constant, K_1k_{+2}, determined from the initial slope, decreased 2.4-fold in the presence of Ficoll70.

5.3.4 Rate of the Actomyosin Weak-to-Strong-Binding Transition

The rate of the weak-to-strong-binding transition, $K_8k`_{+4}$, was measured in the double-mixing experiment (step 4, Figure 5-2). Initially, myosin at various concentrations was rapidly mixed with 100 μM ATP and the reaction was aged in the delay loop for 2 s to populate myosin in the postrecovery state. After the delay, 0.3 μM pyrene actin with 1 mM ADP was rapidly added to the myosin. Pyrene actin fluorescence is sensitive to strong actomyosin binding (58), and we monitored the formation of a strong actomyosin bond via a decrease in pyrene fluorescence. 1 mM ADP was added to quench the reaction. The observed pyrene fluorescence transients were fitted with single-exponential functions (Figure 5-3 C). The obtained dependence of reaction rate constants on the myosin concentration was fitted by a straight line (Figure 5-1 E). The rate of the weak-to-strong-binding transition was determined from the slope of the line and was found to be 2.5-fold smaller in the presence of Ficoll70 than in the noncrowded solution.

5.3.5 ADP Dissociation from Actomyosin

To measure the ADP dissociation constant, $K`_5$, we first premixed 0.5 μM pyrene-labeled actomyosin with various amounts of ADP and then rapidly mixed the solution with ATP (step 5, Figure 5-2). ADP dissociation was monitored via an increase in pyrene fluorescence due to actomyosin dissociation after the dissociation of ADP and

ATP binding. ADP dissociation is a slow process compared with ATP-induced actomyosin dissociation (Figure 5-3 A), and therefore the rate measured in an experiment is determined by the kinetics of ADP dissociation. The observed transients of pyrene fluorescence were fitted with single-exponential functions. The obtained dependencies of the reaction rates of actomyosin dissociation on [ADP] were fitted using the model of competitive inhibition (59) (Figure 5-1 F). We found that $K`_5$ was the same with and without Ficoll70 (Table 5-1). The high affinity of ADP for our myosin construct is in good agreement with the literature data for *D. discoideum* myosin (54).

5.3.6 Structure of Myosin Head

We used FRET (9, 60) to measure the distance between two FRET probes attached to myosin and thus determine the effect of macromolecular crowding on the protein structure. The donor and acceptor probes were attached to K498C (the force-generating region) and A639C (the lower 50 kDa domain) within the myosin head (Figure 5-4), and the interprobe distance in the pre- and postrecovery structural states (M, M*, and M**; Figure 5-2) was measured in a transient kinetics experiment (55). We mixed myosin (M, 10 μM) with the buffer to measure the interprobe distance in the M state, and detected a 0.8 nm interprobe distance reduction in the presence of Ficoll70 (Figure 5-4). We mixed myosin with 300 μM ATP to monitor the formation of the M** state via an increased FRET effect. The interprobe distance and Ficoll70-induced distance change of the M* state were similar to those of the M state. We found a 0.6 nm interprobe distance reduction in the M** structural state in the presence of Ficoll70 (Figure 5-4). The kinetics of the M** state formation determined with the FRET pair was the same as the kinetics of the myosin intrinsic fluorescence change. We conclude that the myosin head assumes a more compact form in a crowded solution than in a

dilute solution to minimize its excluded volume according to Le Chatelier's principle. The observed decrease of the ligands' affinity for myosin in the crowded solution leads us to suggest that the structural change affects the structure or dynamics of the corresponding ligand-binding sites.

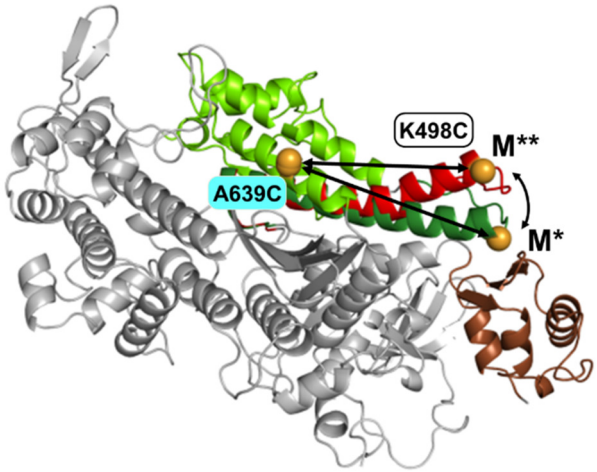

Figure 5-4: The myosin head, with overlay of crystal structures 1FMV (M*) and 1VOM (M**), showing conformational change within force-generating region. Spheres: engineered labeling sites, showing predicted shortening of distance between 639 and 498 (*arrows*) during the recovery stroke.

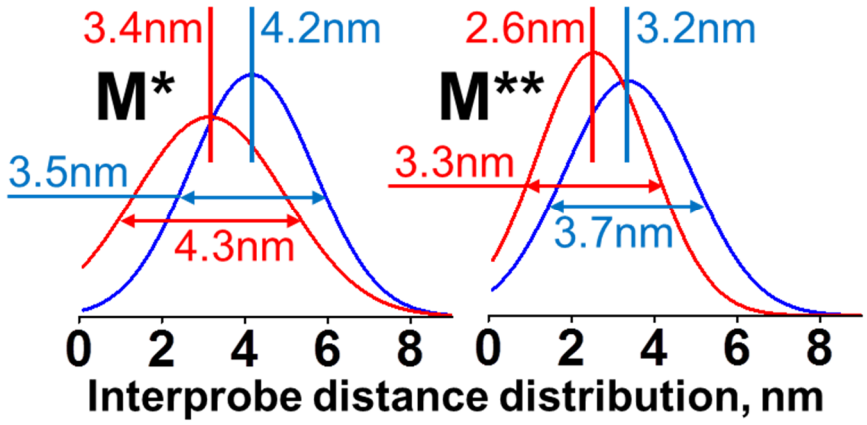

Figure 5-5: Gaussian distance distributions of the FRET pair within myosin head (K498C:A639C), without (*blue*) and with (*red*) Ficoll70 in solution.

5.4 Discussion

According to the excluded-volume theory (45), the rate of the myosin reaction with the ligands actin and ATP is expected to increase in a crowded solution due to the increase in the chemical potential of the solutes. However, we did not observe such a rate increase in our experiments. The observed decrease in the rates of actomyosin and

myosin-nucleotide association indicates that other factors affect the myosin-ligand interaction in a crowded solution. Such factors could include the increased ionic strength of the solution, osmotic pressure, viscosity, and structural changes of myosin head or actin induced by macromolecular crowding. Literature data (61) and our experiments show that the increased ionic strength decreases the rate of actomyosin association. For our *D. discoideum* myosin construct, we found that the rate decrease was two times smaller than the effect of macromolecular crowding. Therefore, the effect of increased ionic strength is not dominant when actomyosin is in crowded conditions. The crowding increases the osmotic pressure, which in turn decreases the rate of the rigor complex formation (for example, in a 30% w/v sucrose solution, the rate decreases fivefold due to an increase in osmotic pressure (62)), but the osmotic pressure produced by 25% w/v Ficoll70 is ~20 times lower than that of the 30% w/v sucrose solution (49), making the effect of the osmotic pressure negligible. Previously, myosin kinetics experiments were performed in the presence of polyethylene glycol (PEG) of different sizes (63-65). One has to distinguish between a globular crowder (Ficoll) and a polymer (PEG), which forms loose mesh in solution (66). PEG affects osmotic pressure, changing the hydration of solutes, and therefore the effects of PEG and Ficoll70 on myosin kinetics could not be compared. For example, addition of Ficoll70 does not change myosin basal ATPase activity, but addition of PEG decreases ATPase activity (64, 65), as does addition of another known osmolate, sucrose (62).

The macroscopic viscosity of 25% w/v Ficoll70 solution is $\eta = 17$ cP (67). Using the Stokes-Einstein relation, we can estimate the coefficient of myosin translational diffusion as 2.5×10^{-12} m^2s^{-1} (assuming for simplicity that the myosin head is a spheroid with a diameter of 10 nm), and that of ATP as 2.5×10^{-11} m^2s^{-1}. The rate of the myosin-ligand binding can be estimated from the Smoluchowski expression, modified with the

statistical weights to account for favorable orientations of interacting molecules (68), $k_{+1} = 4\pi D_{12} R_{12} f_1 f_2$ (where $R_{12} = R_1 + R_2$ is the reaction radius, approximately equal to the sum of the molecular radii of myosin and ligand; $D_{12} = D_1 + D_2$ is the relative coefficient of translational diffusion; and $f_i = (1/4)\sin^2(\theta_i/2)$, i = 1,2 is the geometric steric factor, reflecting the angular size θ_i of the reactive spot of interacting molecules, determined as the ratio of the surfaces of the reactive spot and the whole molecule). For the myosin-ATP interaction, assuming $f_{ATP} \sim 0.5$ and $f_{myosin} = 2.5 \times 10^{-3}$ (the reactive spot on the myosin surface on the order of the size of ATP), $k_{+1}^{-F} = 1.43\ \mu M^{-1}s^{-1}$ without Ficoll70, and $k_{+1}^{+F} = 0.08\ \mu M^{-1}s^{-1}$ with Ficoll70. The estimated k_{+1}^{-F} is an order of magnitude larger than the observed rate constant $K_1 k_{+2}$ (Table 5-1); therefore, the solvent viscosity does not affect the reaction. With Ficoll70, the estimated k_{+1}^{+F} is close to the experimental rate constant, indicating that the solvent viscosity may affect the reaction rate. Interestingly, the obtained values of $K`_1 k`_{+2}$ for the actomyosin-ATP interaction with and without Ficoll70 are close to the calculated values of $k`_{+1}$ ($1.25\ \mu M^{-1}s^{-1}$ and $1.43\ \mu M^{-1}s^{-1}$ without Ficoll70, and $0.09\ \mu M^{-1}s^{-1}$ and $0.08\ \mu M^{-1}s^{-1}$ with Ficoll70), indicating that the ATP binding to actomyosin may be a diffusion-controlled step. For the actomyosin interaction, assuming $f_{actin} = 0.27$ and $f_{myosin} = 0.05$ (taking the actin filament as a cylinder with a diameter of 8.4 nm, and the actomyosin interacting spot to have a 2.3 nm radius (69), $f_{actin} = (1/2)\sin(\theta/2)$, where θ is the angular size of the interaction spot measured from the axis of the cylinder, and a slow diffusion of actin filament, $D_{actin} << D_{myosin}$, one can estimate $k_{+1}^{-F} = 2.5\ \mu M^{-1}s^{-1}$ without Ficoll70 and $k_{+1}^{+F} = 0.15\ \mu M^{-1}s^{-1}$ with Ficoll70. The obtained rate of the actomyosin weak-to-strong binding transition without Ficoll70 is an order of magnitude slower than the calculated diffusion-limited rate, and with Ficoll70 the obtained rate is just three times less than the calculated diffusion-limiting rate, indicating that in the crowded environment the

interaction of actin and myosin may be diffusion controlled. Our electron paramagnetic resonance experiments show that actin structure is not affected by Ficoll70 in solution, but the FRET experiment shows that the myosin head adopts a more compact structural state compared with that in a dilute solution. It is possible that the structural change in the myosin head affects the kinetics of the actomyosin cycle and therefore may change the duty ratio of myosin molecular motor.

5.5 Conclusions

As a result of detailed kinetic studies, we found that the effect of Ficoll70 on myosin cannot be explained by changes in the ligand chemical potential. The increased viscosity of the crowded solution leads to diffusion control over the myosin-ligand interaction. A transient time-resolved Förster resonance energy transfer (TR^2FRET) experiment detected a structural change within the myosin head in the presence of Ficoll70. This structural change could lead to the observed changes in the actomyosin kinetics.

CHAPTER 6: EFFECT OF IONIC STRENGTH ON ACTOMYOSIN INTERACTIONS

6.1 Introduction

The rate of actin and myosin rigor binding depends on the ionic strength of the solution, confirming that actomyosin interaction is electrostatically driven. The dependence of the rate of actin and myosin interaction on the ionic strength of the solution reflects the charge of the interface of the interacting molecules. We used fluorescence of pyrene labeled actin to measure transient kinetics of actomyosin rigor binding in buffered solutions of different ionic strength and constant pH. We used recent data on the structure of actomyosin complex (69) to determine the charge and charge distribution of the actin binding interface of myosin head. The experimental transient kinetics data and the computational analysis were used to compare cellular and muscle myosin in terms of similarities and differences of their actin binding interface.

6.2 Ionic Strength and Debye-Huckel Theory

The ionic strength of a solution is a measure of the concentration of ions in the solution. The ionic compounds (e.g salts), dissociate into ions, when they are dissolved in water. Ionic strength is one of the main characteristics of a solution with dissolved ions, which influences many important properties like, the dissociation or solubility of different salts(70). The molar ionic strength, I, of a solution is a function of the concentration of all ions present in that solution.

$$I = \frac{1}{2}\sum_{i=1}^{n} c_i z_i^2 \qquad (6.1)$$

where one half is because we are including both cations and anions, c_i is the molar concentration of ion i (M, mol/L), z_i is the charge number of that ion, and the sum is taken over all ions in the solution.

The ionic strength is utilized to describe the strong deviations from the ideality typically experienced in ionic solutions via the Debye-Hückel theory(71). The Debye length is inversely proportional to the square root of the ionic strength Figure 6-1.

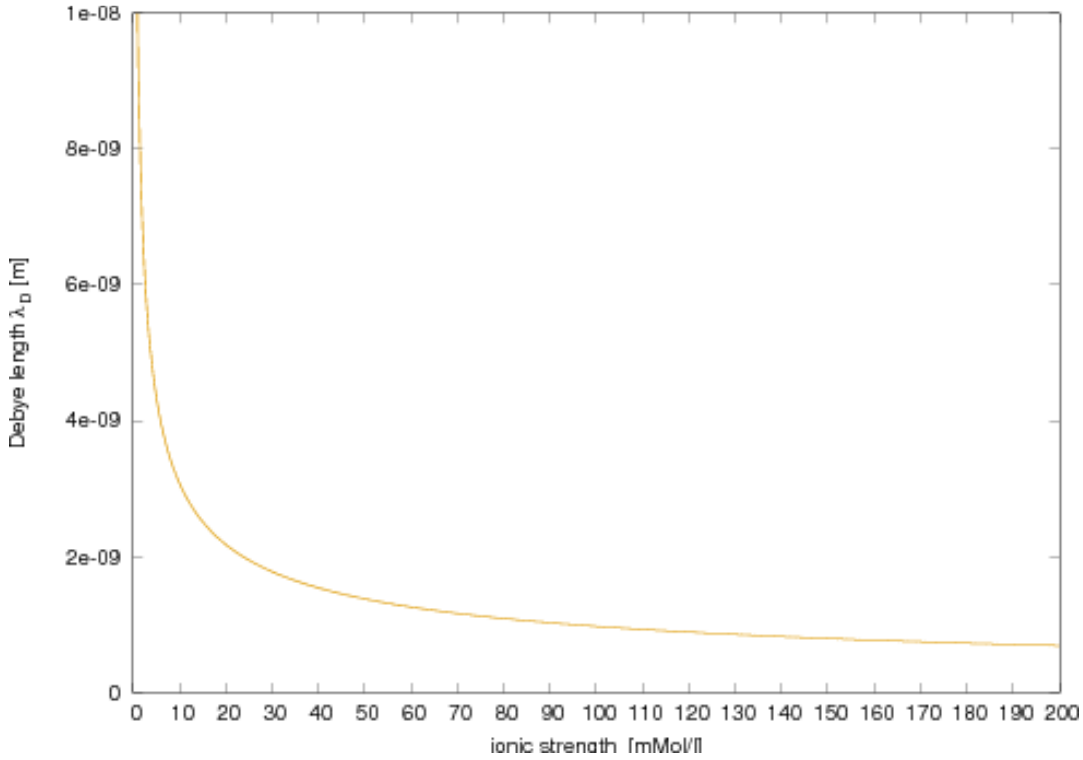

Figure 6-1: The dependence of the Debye length on ion concentration for a 1:1 electrolytic solution.

6.3 Rate of Actomyosin Association Depends on the Ionic Strength

Transient fluorescence of pyrene actin was measured with Bio-Logic SFM-300 stopped flow transient fluorimeter (Bio-Logic Science Instruments SAS, Claix, France), equipped with FC-15 cuvette. The mixing unit dead time is 2.6 ms. All experiments were done at T=20^{o} C. The pyrene fluorescence was excited at 365 nm and detected using a 420 nm cutoff filter. Multiple transients were usually acquired and averaged to improve signal to noise ratio. 8000 points were acquired in each experiment.

The transients obtained in each experiment were fitted globally by the sum of two exponential functions. Both functions, fast and slow, showed dependence on the ionic strength, the dependence of the fast exponential function on the ionic strength is larger.

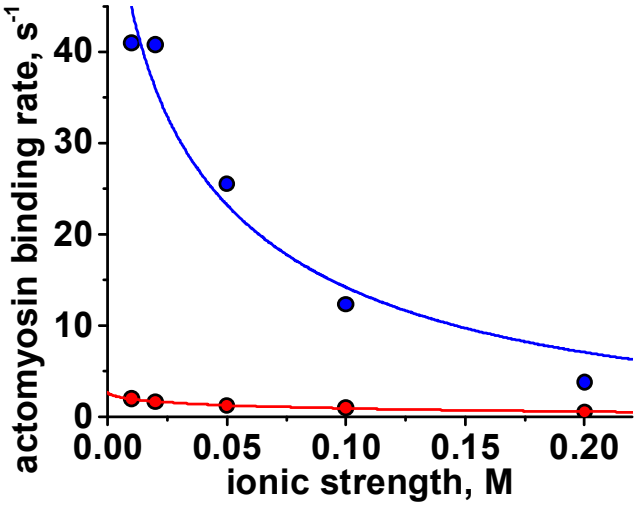

Figure 6-2: The dependence of the rate of actomyosin association on the ionic strength of the solution. Dots, experiment, line, fit to the Debye-Huckel equation, y = exp(A-B*Sqrt(I)), where A is the rate of actomyosin interaction at I = 0.

There is a significant difference between cellular and skeletal myosin II S1 in the dependence of the rate of actomyosin association on the ionic strength of the solution (Figure 6-2), telling that (a) electrostatics play a role in actomyosin interaction, (b) there is a difference in electrostatic charge of these proteins.

6.4 Surface Charge Distribution of Myosin at the Actomyosin Interface

Crystal structures 1FMV.pdb (D. discoideum myosin) and 2MYS (skeletal myosn) were aligned using Pymol. Missed loops were built in Molecular Operating Environment software package, hydrogens were added, and atomic partial charges were calculated using PDB2PQR web server (www.poissonboltzmann.org). The loops of the actin binding interface were determined in (69). All atoms of the actin binding interface were projected on the plane, perpendicular to the line, connecting the center of mass of the molecule and the center of mass of the actin binding interface, using Wolfram

Mathematica as shown in Figure 6-3. Projection of atoms is colored according to the charge of the atom, in the color scheme blue-white red, negative-neutral-positive. Surface charge of myosin at the actomyosin interface is distributed uniformly, without any charged patches for cellular myosin or skeletal myosin (Figure 6-4).

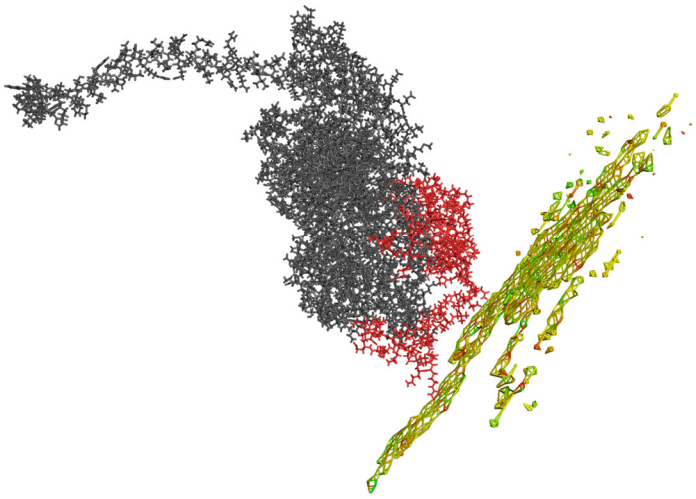

Figure 6-3: Crystal structure of skeletal myosin (2MYS) (gray), actin binding interface [1] (red), and the projection of the actin binding interface on the plane.

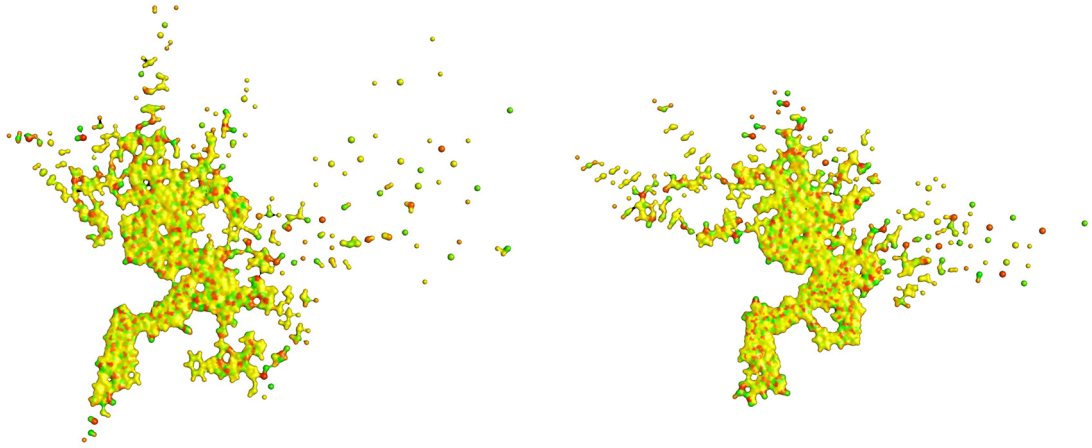

Figure 6-4: Projections of the surface charge of actin binding interface. Left, cellular myosin; right, skeletal myosin. Green, negative charge, red, positive charge, yellow, no charge.

6.5 Surface Charge for Cellular and Skeletal Myosin

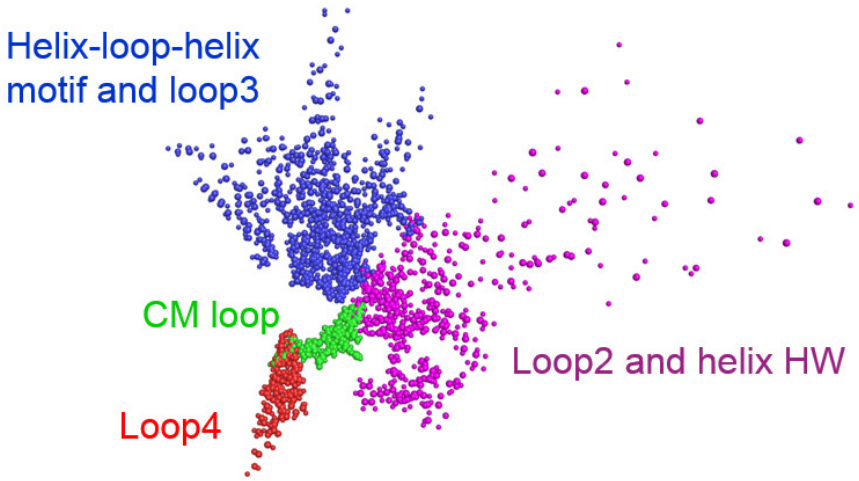

Figure 6-5: Projections of the surface charge of actin binding interface for individual loops.

Total charge of both cellular and skeletal myosin S1 were counted for individual loops as shown in Table 6-1. Absolute value of the charge of the actomyosin binding interface is 2e in cellular myosin and 6e in skeletal myosin. Our experimental data agree that higher absolute value of the surface charge at the binding interface significantly increases the probability of actomyosin binding.

Table 6-1: Total charge of both cellular and skeletal myosin S1 for different loops

Structural element at the actin binding site	Charge	
	Cellular myosin	Skeletal myosin
Loop 4	0e	-2e
CM loop	0e	0e
Helix-loop-helix motif and loop3	0e	0e
Loop2 and helix HW	+2e	+4e
Total absolute charges	2e	6e

6.6 Discussion

Using the Stokes-Einstein relation, the coefficient of myosin translational diffusion can be estimated as $2.5 \cdot 10^{-12}$ $m^2 s^{-1}$ (assuming for simplicity the myosin head to be a spheroid with the diameter of 10 nm). The rate of the myosin-ligand binding can be estimated from the Smoluchowski expression, modified with the statistical weights to

account for favorable orientations of interacting molecules (72), $k_{A+M} = 4\pi D_{12} R_{12} f_1 f_2$ (where $R_{12} = R_1 + R_2$ is the reaction radius, approximately equal to the sum of the molecular radii of myosin and ligand, $D_{12}=D_1+D_2$ is the relative coefficient of translational diffusion, and $f_i=(1/4)\sin^2(\theta_i/2)$, i=1,2, is the geometric steric factor, reflecting the angular size θ_i of the reactive spot of interacting molecules, determined as the ratio of the surfaces of the reactive spot and the whole molecule). For actomyosin interaction, we assume $f_{actin} = 0.27$ and $f_{myosin} = 0.05$, taking actin filament as a cylinder with the diameter of 8.4 nm, and the actomyosin interacting spot to have a 2.3 nm radius (69), $f_{actin}=(1/2)\sin(\theta/2)$, where θ is the angular size of the interaction spot measured from the axis of the cylinder. Assuming slow diffusion of actin filament, $D_{actin} << D_{myosin}$, one can estimate $k_{A+M} = 2.5\ \mu M^{-1}s^{-1}$. Experimentally measured actomyosin reaction rate for cellular myosin is 2 $\mu M^{-1}s^{-1}$ - 0.6 $\mu M^{-1}s^{-1}$ in the range of the solution's ionic strength 19mM – 209mM, which is not far from the estimated rate of diffusion.

At the micromolar concentrations of myosin and actin in solution, the distance between molecules is in the order of 100nm, much larger than the Debye radius (2.2 nm for 20mM KCl and 0.7 nm for 200mM KCl), therefore we expect no long range electrostatic interactions between molecules, only Brownian diffusion. We observed a dependence of the rate of actomyosin interaction on the ionic strength, therefore electrostatics plays a role in the interaction. The size of myosin molecule (radius 5nm) is larger than the Debye radius, therefore only local surface charge is important for actomyosin interaction, not a total charge of the molecule. High ionic strength of the solution decreases the Debye radius, and therefore decreases the time when surface electrostatics can play a role in the actomyosin interaction. Our experimental data prove that higher absolute value of the surface charge at the binding interface significantly increases the probability of actomyosin binding.

6.7 Conclusion

Our study shows that two parameters determine the probability of actomyosin binding, the Debye radius (determines the time actin and myosin surface electrostatics can play a role in the interaction), and surface electric charge of the binding site. We hypothesize that during the time when myosin and actin at the distance of the Debye radius or close, the rotational diffusion positions actin and myosin. The role of surface electric charges is to lock the right actomyosin conformation, or “guide” rotational diffusion toward the right actomyosin conformation.

CHAPTER 7: CONCLUSIONS

In this dissertation work, we have successfully used steady state myosin ATPase activity measurements, myosin intrinsic fluorescence, fluorescence of pyrene labeled actin and home-built transient time-resolved Förster resonance energy transfer to monitor myosin and actomyosin kinetics. we have examined actomyosin regulation by environments including (a) metal ions, complexed with ATP, (b) crowding of actomyosin environment, and (c) ionic strength of actomyosin solution.

In the first study of metal ions complexed with ATP, we have found that metal cation controls the rate limiting step of myosin ATPase. It is the reverse recovery stroke and the phosphate release for magnesium, myosin.ADP isomerization and ADP release for manganese and the absence of well defined reaction limiting step for calcium. Actin binding to myosin.ADP and actin activation of myosin ATPase do not depend on metal cation complexed with ATP. The rate of myosin conformational changes upon interaction with nucleotide depends on the ionic radius of metal cation. The rate of nucleotide binding to and dissociation from myosin and actomyosin depends on metal cation coordination number.

Secondly, we studied macromolecular crowding modulates the actomyosin interaction in solution. The overall rate of the actomyosin cycle increases in a crowded solution. The myosin head adopts a more compact conformation than it does in a dilute solution to minimize the excluded volume. Crowding-induced increase of solution viscosity modulates the interaction of the solutes, and the observed decrease in the

reaction rates of the myosin-actin and myosin-ATP interactions agrees well with the calculated values of the diffusion-controlled reaction rates.

In the third study of ionic strength of actomyosin solution, we observed a dependence of the rate of actomyosin interaction on the ionic strength, therefore electrostatics plays a role in the interaction. We found two parameters determine the probability of actomyosin binding, the Debye radius, and surface electric charge of the binding site. The Debye radius determines the distance between myosin and actin, where electrostatic interactions take place. Increase of the ionic strength of the solution decreases the Debye radius, and therefore, the probability of actomyosin binding. And there is a significant difference between cellular and skeletal myosin II S1 in the dependence of the rate of actomyosin association on the ionic strength of the solution. Our experimental data prove that higher absolute value of the surface charge at the binding interface significantly increases the probability of actomyosin binding.

In summary, the results of this study suggest that cross-bridge kinetics, and therefore muscle performance, significantly depends on intracellular environments.

REFERENCES

1. Bustamante C, Chemla YR, Forde NR, & Izhaky D (2004) Mechanical processes in biochemistry. *Annual Review of Biochemistry* 73(1):705-748.

2. Hodge T, Jamie M, & Cope TV (2000) A myosin family tree. *Journal of Cell Science* 113:3353-3354.

3. Fischer S, Windshugel B, Horak D, Holmes KC, & Smith JC (2005) Structural mechanism of the recovery stroke in the myosin molecular motor. *Proceedings of the National Academy of Sciences* 102:6873-6878.

4. Lymn RW & Taylor EW (1971) Mechanism of adenosine triphosphate hydrolysis by actomyosin. *Biochemistry* 10:4617-4624.

5. Fey P, Kowal AS, Gaudet P, Pilcher KE, & Chisholm RL (2007) Protocols for growth and development of Dictyostelium discoideum. *Nature Protocols* 2(6):10.

6. Ashworth JM & Watts* DJ (1970) Metabolism of the cellular slime mould Dictyostelium discoideum grown in axenic culture. *Biochem J* 119(2):8.

7. Korman VL, Anderson SEB, Prochniewicz E, Titus MA, & Thomas DD (2006) Structural Dynamics of the Actin–Myosin Interface by Site-directed Spectroscopy. *Journal of Molecular Biology* 356(5):1107-1117.

8. Agafonov RV*, et al.* (2009) Structural dynamics of the relay helix during the myosin recovery stroke by time-resolved EPR and FRET. *Proc Natl Acad Sci U S A* 106(51):21625-21630.

9. Nesmelov YE*, et al.* (2011) Structural kinetics of myosin by transient time-resolved FRET. *Proceedings of the National Academy of Sciences of the United States of America* 108(5):1891-1896.

10. Manstein DJ & Hunt DM (1995) Over-expression of myosin motor domains in Dictyostelium: screening of transformants and purification of affinity tagged protein. *J. Muscle Res. Cell Motil.* 16:325-332.

11. Tkachev YV, Ge J, Negrashov IV, & Nesmelov YE (2013) Metal cation controls myosin and actomyosin kinetics. *Protein Science* 22(12):9.

12. Astashkin AV & Nesmelov YE (2012) Mn2+–Nucleotide Coordination at the Myosin Active Site As Detected by Pulsed Electron Paramagnetic Resonance. *J Phys Chem B* 116(46):13655–13662.

13. Pollard TD (1982) Myosin Purification and Characterization. *Methods in Cell Biology*, (Elsevier), Vol 24.

14. Margossian SS & Lowey S (1982) Preparation of myosin and its subfragments from rabbit skeletal muscle. *Methods in Enzymology* 85:55-71.

15. Weeds AG & Taylor RS (1975) Separation of subfragment-1 isoenzymes from rabbit skeletal muscle myosin. *Nature* 257(5521):54-56.

16. Strzelecka-Golaszewska H, Prochniewicz E, Nowak E, Zmorzynski S, & Drabikowski W (1980) Chicken-gizzard actin: polymerization and stability. *Eur J Biochem* 104(1):41-52.

17. Drabikowski W & Gergely J (1962) The effect of the temperature of extraction on the tropomyosin content in actin. *The Journal of Biological Chemistry* 237(11):3412-3417.

18. Mommaerts WF (1952) The molecular transformations of actin. I. Globular actin. *J Biol Chem* 1952(1):445-457.

19. Houk TW, Jr. & Ue K (1974) The measurement of actin concentration in solution: a comparison of methods. *Anal Biochem* 62(1):66-74.

20. Takagi Y*, et al.* (2008) Human myosin Vc is a low duty ratio, nonprocessive molecular motor. *J Biol Chem* 283(13):8527-8537.

21. Shapiro AL, Vinuela E, & Maizel JV (1967) Molecular weight estimation of polypeptide chains by electrophoresis in SDS-polyacrylamide gels. *Biochem Biophys Res Commun* 28(5):6.

22. Lanzetta PA, Alvarez LJ, Reinach PS, & Candia OA (1979) An improved assay for nanomole amounts of inorganic phosphate. Anal Biochem. *Anal Biochem* 100(1):95-97.

23. Petushkova EV, Grishin MN, Baranova LA, & Guliaev NN (1988) [Increased substrate selectivity during transition from Ca2+-activated to K+,EDTA-activated nucleoside triphosphatase activity of heavy meromyosin]. *Biokhimiia (Moscow, Russia)* 53(1):143-149.

24. Pate E, Franks-Skiba K, White H, & Cooke R (1993) The use of differing nucleotides to investigate cross-bridge kinetics. *J Biol Chem* 268(14):10046-10053.

25. White HD, Belknap B, & Jiang W (1993) Kinetics of binding and hydrolysis of a series of nucleoside triphosphates by actomyosin-S1. Relationship between solution rate constants and properties of muscle fibers. *J Biol Chem* 268(14):10039-10045.

26. Regnier M, Rivera AJ, Chen Y, & Chase PB (2000) 2-deoxy-ATP enhances contractility of rat cardiac muscle. *Circulation research* 86(12):1211-1217.

27. Ikebe M, Inoue A, & Tonomura Y (1980) Reaction mechanism of Mn2+-ATPase of acto-H-meromyosin in 0.1 M KCl at 5 degrees C: evidence for the Lymn-Taylor mechanism. *Journal of biochemistry* 88(6):1653-1662.

28. Inoue A, Ikebe M, & Tonomura Y (1980) Mechanism of the Mg2+- and Mn2+-ATPase reactions of acto-H-meromyosin and acto-subfragment-1 in the absence

of KCl at room temperature: direct decomposition of the complex of myosin-P-ADP with f-actin. *Journal of biochemistry* 88(6):1663-1677.

29. Peyser YM, Ben-Hur M, Werber MM, & Muhlrad A (1996) Effect of divalent cations on the formation and stability of myosin subfragment 1-ADP-phosphate analog complexes. *Biochemistry* 35(14):4409-4416.

30. Burton K, White H, & Sleep J (2005) Kinetics of muscle contraction and actomyosin NTP hydrolysis from rabbit using a series of metal-nucleotide substrates. *The Journal of physiology* 563(Pt 3):689-711.

31. Bagshaw CR (1975) The kinetic mechanism of the manganous ion-dependent adenosine triphosphatase of myosin subfragment 1. *FEBS letters* 58(1):197-201.

32. Roman V. Agafonov IVN, Yaroslav V. Tkachev, Sarah E. Blakely, Margaret A. Titus, David D. Thomas, Yuri E. Nesmelov (2009) Structural dynamics of the relay helix during the myosin recovery stroke by time-resolved EPR and FRET. *Proceedings of the National Academy of Sciences* 106(51):21625-21630.

33. Bagshaw CR & Trentham DR (1974) The characterization of myosin-product complexes and of product-release steps during the magnesium ion-dependent adenosine triphosphatase reaction. *Biochem J* 141(2):331-349.

34. Werber MM, Szent-Gyorgyi AG, & Fasman GD (1972) Fluorescence studies on heavy meromyosin-substrate interaction. *Biochemistry* 11(15):2872-2883.

35. Reshetnyak YK*, et al.* (2000) The identification of tryptophan residues responsible for ATP-induced increase in intrinsic fluorescence of myosin subfragment 1. *Journal of biomolecular structure & dynamics* 18(1):113-125.

36. Malnasi-Csizmadia A, Woolley RJ, & Bagshaw CR (2000) Resolution of conformational states of Dictyostelium myosin II motor domain using tryptophan (W501) mutants: implications for the open-closed transition identified by crystallography. *Biochemistry* 39(51):16135-16146.

37. Yengo CM, Chrin LR, Rovner AS, & Berger CL (2000) Tryptophan 512 is sensitive to conformational changes in the rigid relay loop of smooth muscle myosin during the MgATPase cycle. *J Biol Chem* 275(33):25481-25487.

38. Kovacs M, Malnasi-Csizmadia A, Woolley RJ, & Bagshaw CR (2002) Analysis of nucleotide binding to Dictyostelium myosin II motor domains containing a single tryptophan near the active site. *J Biol Chem* 277(32):28459-28467.

39. Ritchie MD, Geeves MA, Woodward SK, & Manstein DJ (1993) Kinetic characterization of a cytoplasmic myosin motor domain expressed in Dictyostelium discoideum. *Proceedings of the National Academy of Sciences of the United States of America* 90(18):8619-8623.

40. Gyimesi M*, et al.* (2008) The mechanism of the reverse recovery step, phosphate release, and actin activation of Dictyostelium myosin II. *J Biol Chem* 283(13):8153-8163.

41. Deacon JC, Bloemink MJ, Rezavandi H, Geeves MA, & Leinwand LA (2012) Erratum to: Identification of functional differences between recombinant human α and β cardiac myosin motors. *Cellular and Molecular Life Sciences* 69(24):4239-4255.

42. De La Cruz EM & Michael Ostap E (2009) Chapter 6 Kinetic and Equilibrium Analysis of the Myosin ATPase. *Methods in Enzymology*, (Academic Press), Vol Volume 455, pp 157-192.

43. Segel IH (1976) *Biochemical Calculations* (Wiley, New York) 2nd Ed.

44. Reubold TF, Eschenburg S, Becker A, Kull FJ, & Manstein DJ (2003) A structural model for actin-induced nucleotide release in myosin. *Nature structural biology* 10(10):826-830.

45. Minton AP (1983) The effect of volume occupancy upon the thermodynamic activity of proteins: some biochemical consequences. *Mol. Cell. Biochem.* 55:22.

46. Ellis RJ (2001) Macromolecular crowding: obvious but underappreciated. *Trends in biochemical sciences* 26(10):597-604.

47. Elcock AH (2010) Models of macromolecular crowding effects and the need for quantitative comparisons with experiment. *Curr. Opin. Struct. Biol.* 20:11.

48. Wenner JR & Bloomfield VA (1999) Crowding effects on EcoRV kinetics and binding. *Biophysical journal* 77(6):3234-3241.

49. Lopez CJ, Fleissner MR, Guo Z, Kusnetzow AK, & Hubbell WL (2009) Osmolyte perturbation reveals conformational equilibria in spin-labeled proteins. *Protein science : a publication of the Protein Society* 18(8):1637-1652.

50. Dhar A*, et al.* (2010) Structure, function, and folding of phosphoglycerate kinase are strongly perturbed by macromolecular crowding. *Proceedings of the National Academy of Sciences of the United States of America* 107(41):17586-17591.

51. Wang Y, Sarkar M, Smith AE, Krois AS, & Pielak GJ (2012) Macromolecular crowding and protein stability. *Journal of the American Chemical Society* 134(40):16614-16618.

52. Garrigos M, Morel JE, & Garcia de la Torre J (1983) Reinvestigation of the shape and state of hydration of the skeletal myosin subfragment 1 monomer in solution. *Biochemistry* 22(21):4961-4969.

53. Woodward SK, Geeves MA, & Manstein DJ (1995) Kinetic characterization of the catalytic domain of Dictyostelium discoideum myosin. *Biochemistry* 34(49):16056-16064.

54. Kurzawa SE, Manstein DJ, & Geeves MA (1997) Dictyostelium discoideum myosin II: characterization of functional myosin motor fragments. *Biochemistry* 36(2):317-323.

55. Tkachev YV, Ge J, Negrashov IV, & Nesmelov YE (2013) Metal cation controls myosin and actomyosin kinetics. *Protein science : a publication of the Protein Society* 22(12):1766-1774.

56. De La Cruz EM, Wells AL, Rosenfeld SS, Ostap EM, & Sweeney HL (1999) The kinetic mechanism of myosin V. *Proceedings of the National Academy of Sciences of the United States of America* 96(24):13726-13731.

57. Malnasi-Csizmadia A*, et al.* (2001) Kinetic resolution of a conformational transition and the ATP hydrolysis step using relaxation methods with a Dictyostelium myosin II mutant containing a single tryptophan residue. *Biochemistry* 40(42):12727-12737.

58. De La Cruz EM & Ostap EM (2009) Kinetic and equilibrium analysis of the myosin ATPase. *Methods in enzymology* 455:157-192.

59. Segel IH (1976) *Biochemical Calculations: How to Solve Mathematical Problems in General Biochemistry* (Wiley, New York).

60. Agafonov RV*, et al.* (2009) Structural dynamics of the myosin relay helix by time-resolved EPR and FRET. *Proceedings of the National Academy of Sciences of the United States of America* 106(51):21625-21630.

61. Siemankowski RF & White HD (1984) Kinetics of the interaction between actin, ADP, and cardiac myosin-S1. *The Journal of biological chemistry* 259(8):5045-5053.

62. Jackson del R, Jr.*, et al.* (2014) Sucrose increases the activation energy barrier for actin-myosin strong binding. *Archives of biochemistry and biophysics* 552-553:74-82.

63. Highsmith S, Duignan K, Cooke R, & Cohen J (1996) Osmotic pressure probe of actin-myosin hydration changes during ATP hydrolysis. *Biophysical journal* 70(6):2830-2837.

64. Highsmith S, Duignan K, Franks-Skiba K, Polosukhina K, & Cooke R (1998) Reversible inactivation of myosin subfragment 1 activity by mechanical immobilization. *Biophysical journal* 74(3):1465-1472.

65. Grazi E, Cintio O, Magri E, & Trombetta G (1999) Reversible inactivation of myosin subfragment-1 activity by mechanical immobilization: a reappraisal. *Biophysical journal* 76(6):3349-3350; author reply 3351.

66. Sozanski K*, et al.* (2015) Small Crowders Slow Down Kinesin-1 Stepping by Hindering Motor Domain Diffusion. *Physical review letters* 115(21):218102.

67. Onishi H, Mikhailenko SV, & Morales MF (2006) Toward understanding actin activation of myosin ATPase: the role of myosin surface loops. *Proceedings of the National Academy of Sciences of the United States of America* 103(16):6136-6141.

68. Temkin SI & Yakobson BI (1984) Diffusion-controlled reactions of chemically anisotropic molecules. *J. Phys. Chem.* 88:4.

69. Behrmann E*, et al.* (2012) Structure of the rigor actin-tropomyosin-myosin complex. *Cell* 150(2):327-338.

70. Vicente MESd (2004) The Concept of Ionic Strength Eighty Years after Its Introduction in Chemistry. *J. Chem. Educ* 81(5):4.

71. Debye P & Hückel E (1923) The theory of electrolytes. I. Lowering of freezing point and related phenomena. *Physikalische Zeitschrift* 24(9):12.

72. Temkin SI & Yakobson BI (1984) Diffusion-Controlled Reactions of Chemically Anisotropic Molecules. *J Phys Chem-Us* 88(13):2679-2682.

LIST OF PUBLICATIONS AND PRESENTATIONS

Journal Publications

1. **J Ge**, SD Bouriyaphone, TA Serebrennikova, AV Astashkin, YE Nesmelov, *Macromolecular Crowding Modulates Actomyosin Kinetics*, **Biophysical Journal** 111 (1), 178 (2016).

2. YV Tkachev, **J Ge**, IV Negrashov, YE Nesmelov, *Metal cation controls myosin and actomyosin kinetics*, **Protein science** 22 (12), 1766 (2013).

3. *Electrostatics of Actomyosin Interface and the Rate of Rigor Binding*, to be submitted.

4. *The charge of metal cation controls phosphate release in myosin ATPase*, to be submitted.

Conference Proceedings

1. **J Ge**, B Ambil, F Huang, YE Nesmelov, *Electrostatics of Actomyosin Interface and the Rate of Rigor Binding*, Biophysical Journal 110 (3), 615a (**2016 BPS**).

2. **J Ge**, SD Bouriyaphone1, YE Nesmelov, *Macromolecular Crowding Modulates Cross-Bridge Performance*, Biophysical Journal 108 (2), 301a (**2015 BPS**, awarded).

3. **J Ge**, SD Bouriyaphone1, YE Nesmelov, *Macromolecular Crowding Increases Cross-Bridge Performance via Reduction of ADP Affinity to Acto-Myosin*, Biophysical Journal 108(2):301a (**2015 BPS**).

4. **J Ge**, YV Tkachev, YE Nesmelov, *Position of Phenylalanine in the Relay Loop is Important for Myosin Motor Action*, Biophysical Journal 106 (2), 157a (**2014 BPS**).

5. **J Ge**, YV Tkachev, YE Nesmelov, *Rapid freeze for pulsed EPR studies of ATP hydrolysis*, (**2012 ACS Southeastern Regional Meeting**, awarded).

6. YV Tkachev, **J Ge**, YE Nesmelov, *Myosin kinetics modulation by coordinated divalent cation*, (**2014 Modern Chemical Physics**).

7. YV Tkachev, **J Ge**, YE Nesmelov, *Effect of Divalent Metal Cation on Actomyosin ATPase Kinetics*, Biophysical Journal 104 (2), 307a (**2013 BPS**).